Reconstruction of Hourly All-Weather Land Surface Temperature by Integrating Reanalysis Data and Thermal Infrared Data From Geostationary Satellites (RTG)

Lirong Ding, Ji Zhou, Zhao-Liang Li, Jin Ma, Chunxiang Shi, Shuai Sun, Ziwei Wang

Reconstruction of Hourly All-Weather Land Surface Temperature by Integrating Reanalysis Data and Thermal Infrared Data from Geostationary Satellites (RTG)

Lirong Ding, Ji Zhou, Zhao-liang Li, Jin Ma, Chunxiang Shi, Shuai Sun, and Ziwei Wang

***Abstract*—Thermal infrared (TIR) land surface temperature (LST) products derived from geostationary satellites have a high temporal resolution in a diurnal cycle, but they have many missing values under cloudy-sky conditions. Therefore, it is pressing to obtain all-weather LST (AW LST) with a high temporal resolution by filling the gap of TIR LST. In this study, a method integrating reanalysis data and TIR data from geostationary satellites (RTG) was proposed for reconstructing hourly AW LST. Then, taking the Tibetan Plateau, which is a focus of climate change as a case, RTG was applied to the Chinese Fengyun-4A (FY-4A) TIR LST and China Land Surface Data Assimilation System (CLDAS) data. Validation based on the *in-situ* LST shows that the accuracy of the AW LST is better than the FY-4A LST and CLDAS LST under clear-sky, cloudy-sky, and all-weather conditions. The mean RMSEs are 3.02 K for clear-sky conditions, 3.94 K for cloudy-sky conditions, and 3.57 K for all-weather conditions. Uncertainty and coarse resolution of the original FY-4A and CLDAS data affect the accuracy of the obtained AW LST. The results of the LST time series comparison also show that the reconstructed AW LST is consistent with *in-situ* LST. The reconstructed AW LST also has good image quality and provides reliable spatial patterns. RTG is practical in obtaining high temporal resolution AW LST from the Chinese FY-4A to satisfy related applications. It can also be extended to other geostationary satellites and reanalysis datasets.**

***Index Terms*—All-weather, geostationary satellite, high-temporal resolution, land surface temperature, thermal infrared.**

I. Introduction

LAND surface temperature (LST) plays a vital role in the interactions between the earth's surface and atmosphere [1]–[4]. It is an essential input and basic parameter in many applications, including global climate change studies [5], [6], ecological monitoring and assessment [7]–[10], hydrological process simulation [11], [12], and surface radiation balance and energy budget modeling [13], [14]. Thus, as the global climate and land surface change continuously, LST is becoming increasingly crucial in related areas.

The accurate acquisition of LST over large areas is extremely important. Since remote sensing has the advantages of low cost, wide spatial coverage, and frequent observation, it has become the main way for LST acquisition [15]–[17]. The LST estimation using satellite remote sensing has become a long-standing and classical topic for remote sensing science. With the continuous development of studies in the geoscience field, acquiring all-weather (AW) LST is increasingly pressing [18], [19]. However, current widely-used satellite thermal infrared (TIR) LSTs are significantly affected by clouds and only available for clear-sky conditions [20]. Statistics showed that the global cloud coverage is generally above 50%, especially in climate-sensitive regions such as the Amazon Basin and the Tibetan Plateau [21]. Clouds are the main cause of missing TIR LSTs, and they further reduce the temporal resolution. Therefore, to obtain AW LST data, an effective way is to fill the spatial gaps caused by clouds in TIR LST products.

Studies on how to obtain AW LST based on satellite TIR observations can be classified into two broad categories: (i) reconstruction of cloudy-sky LST based on effective observation and (ii) integration of multi-source data. The spatiotemporal interpolation and energy balance-based methods are two typical ways for the reconstruction of cloudy-sky LST. Among them, the spatiotemporal interpolation-based methods include time-weighted interpolation, spatial-weighted interpolation, and spatiotemporal-weighted interpolation algorithms.

Manuscript received; revised; accepted. This work was supported by the National Natural Science Foundation of China under Grants 41871241, 42271387, and 42201417, by the Fundamental Research Funds for the Central Universities of China, University of Electronic Science and Technology of China under Grant ZYGX2019J069, and by the China Scholarship Council. *(Corresponding author: Ji Zhou)*

L. Ding is with the School of Resources and Environment, University of Electronic Science and Technology of China, Chengdu 611731, China; ICube (UMR 7357), UdS, CNRS, 300 Bld Sebastien Brant, CS 10413, Illkirch 67412, France (e-mail: dlryouxiang@163.com).

J. Zhou, J. Ma, and Z. Wang are with the School of Resources and Environment, University of Electronic Science and Technology of China, Chengdu 611731, China (e-mail: jzhou233@uestc.edu.cn; jin.ma@uestc.edu.cn; wangzw@std.uestc.edu.cn).

Z.-L. Li is with the ICube (UMR 7357), UdS, CNRS, 300 Bld Sebastien Brant, CS 10413, Illkirch 67412, France; the Key Laboratory of Agricultural Remote Sensing, Ministry of Agriculture/Institute of Agricultural Resources and Regional Planning, Chinese Academy of Agricultural Sciences, Beijing 100081, China (e-mail: lizl@unistra.fr).

C. Shi and S. Sun are with the National Meteorological Information Center, China Meteorological Administration, Beijing 100081, China (e-mail: shicx@cma.gov.cn; sunshuai@cma.gov.cn).

The time-weighted interpolation-based algorithms usually use multi-temporal LSTs information in the same region to reconstruct cloudy-sky LSTs. They mainly include linear time interpolation, time Fourier analysis, harmonic analysis, and wavelet transform [22]–[25]. The spatial-weighted interpolation-based algorithms mainly use valid LSTs to recover the missing LSTs by assuming that valid LSTs and missing LSTs have the same statistical and geometric structures. Geo-statistics, spline functions, kriging interpolation, and regression tree analysis are all common approaches in spatial interpolation, and the clear-sky LST is used as the input parameter [26], [27]. Spatiotemporal-weighted interpolation utilizes more observation information and considers the relationship between valid LST observations and target missing pixels from both the spatial and temporal dimensions [28]–[31]. Thus, this approach is generally more stable and effective than the previous two [32]. Spatiotemporal interpolation does not consider the LST difference resulting from the radiation difference between the cloudy-sky and clear-sky pixels. The obtained LST with spatiotemporal interpolation is not the real LST under cloudy-sky conditions but a hypothetical clear-sky LST since they neglect the cloud effect. In contrast, the energy balance (EB)-based interpolation considers the radiation difference and further corrects the LST under the cloudy sky [23], [33], [34]. To take EB into account implicitly, Zhao and Duan [35] used the random forest (RF) to establish a mapping relationship among the clear-sky LST and surface parameters, terrain parameters, and accumulated solar radiation.

Integrating TIR data and other types of data, such as passive microwave (PMW) data or reanalysis data, is another effective routine for obtaining the AW LST. In previous studies, the integration of TIR LST and PMW observations has been widely adopted to obtain the AW LST. For example, Duan et al. [36] reported that the elevation differences of Moderate Resolution Imaging Spectroradiometer (MODIS) pixels within an Advanced Microwave Scanning Radiometer-Earth Observing System sensor (AMSR-E) pixel determine the LST differences. They downscaled the AMSR-E LST using elevation data and fused the downscaled AMSR-E LST with the MODIS LST to obtain the AW LST. Zhang et al. [37] proposed a so-called TCD method based on the temporal component decomposition for estimating the 1-km resolution AW LST by merging TIR and PMW satellite observations. In TCD, LST is first divided into the annual temperature component (T_{ATC}), diurnal temperature component (T_{DTC}), and weather temperature component (T_{WTC}); then, the all-weather T_{ATC}, T_{DTC}, and T_{WTC} are calculated based on the TIR and PMW LSTs, respectively; finally, each component is determined and optimized according to their characteristics, and then the optimized components are superimposed to obtain the AW LST. In addition, Xu et al. [38] used Bayesian maximum entropy to downscale the AMSR-E LST and then merged the downscaled AMSR-E LST with MODIS LST to obtain the AW LST with a 1-km resolution for the Tibetan Plateau and Heihe River Basin. Zhang et al. [39] used the Microwave Radiation Imager (MWRI) brightness temperature (BT) data from the Chinese Fengyun 3B (FY-3B) to reconstruct the AMSR-E PMW BTs within the period of missing data (from 2011 to 2012) based on singular spectrum decomposition (SSA). They integrated the reconstructed PMW BT and MODIS LST to obtain the AW LST. Xu and Cheng [40] proposed a new method to fuse the MODIS TIR LST and downscaled PMW LST based on a cumulative distribution function and multiresolution Kalman filtering. In the processing, the Empirical Orthogonal Functions (EOF) interpolation was used to fill the PMW LST strips. However, PMW data with a high temporal resolution is not currently available; thus, this method may be not practical for TIR LST from geostationary satellites.

Integrating satellite TIR LST and reanalysis data is another approach of multi-source data integration for obtaining the AW LST. However, related studies are still rare. Based on the advantages of the enhanced spatial and temporal adaptive reflectance fusion model (ESTARFM) in the data fusion, Long et al. [41] integrated the China Land Surface Data Assimilation System (CLDAS) LST and MODIS LST to estimate the 1-km resolution AW LST. This study provides a practical way for the integration of TIR data and reanalysis data to obtain the AW LST, which has a stable accuracy (2.37–3.98 K) and image quality while significantly reducing the spatial gaps in the TIR LST. This method has good extendibility to other data sources and other areas. Based on an improved LST temporal decomposition model, Zhang et al. proposed a reanalysis data and TIR remote sensing data merging (RTM) method to reconstruct the AW LST [42]. This method was further used to generate a 22-year daily 1-km AW LST dataset for the Chinese landmass and its surrounding areas (TRIMS LST). The RMSEs of TRIMS LST vary from 1.52 K to 3.71 K for the Heihe River Basin, Northeast China, North China, and South China.

Most previous studies on the AW LST focused on polar-orbiting satellites, while few studies have explored the estimation of high temporal resolution AW LST based on the geostationary satellites [34]. The LST from geostationary satellites has the advantage of high frequency in a diurnal cycle. Therefore, filling the TIR LST with the geostationary satellite to obtain the high temporal resolution AW LST is crucial for characterizing the diurnal variations in many surface processes, such as surface evapotranspiration and urban heat island effect [43], [44]. Especially for the Tibetan Plateau, the AW LST with high temporal resolution can largely strengthen the understanding of the diurnal characteristics of the interaction between the earth's surface and the atmosphere. However, to the best of our knowledge, relevant studies are still rare.

Both geostationary satellite data and reanalysis data have the advantage of high temporal resolution. Thus, it is possible to integrate these two data to obtain the hourly AW LST. In this context, we aim to propose a method for integrating reanalysis data and TIR data from the geostationary satellites (RTG) to reconstruct the hourly AW LST in this study. In RTG, the LST is decomposed into a normal component (NC) and an abnormal component (AC). The NC under all-weather conditions is fitted based on the annual temperature cycle model (ATC), and it is further filled and corrected through the Random Forest (RF) and the diurnal temperature cycle model (DTC). AC is estimated based on the temporal correction of all-weather AC

provided by reanalysis data. Then, with the Chinese Fengyun-4A (FY-4A) TIR LST and CLDAS data, we apply the RTG to the Tibetan Plateau for reconstructing hourly all-weather LSTs. In the end, the obtained hourly AW LST is validated with the *in-situ* LST at six ground sites. This paper is organized as follows: Section II describes the study area and datasets; Section III summarizes the AW LST reconstruction method (RTG); Section IV presents the reconstruction results for the hourly AW LST and discusses the possible reasons affecting the accuracy of AW LST; Section V provides the overall conclusions.

II. Study Area and Datasets

A. Study Area

The Tibetan Plateau (TP) is selected as the study area since it exerts an extraordinary influence on the climate of the surrounding area and even the globe. Specifically, the spatial extent of the study area is 73-106°E and 23-40°N (Fig. 1) and has an average elevation of over 4,000 m. Notably, the elevation changes sharply in the southeastern part of the TP. The complex terrain of the TP induces complex surface characteristics and atmospheric conditions. A large area of glaciers lies on the western and southeastern parts of TP, where many rivers in Asia rise. Thus it is also known as the "Asian water tower" [45], [46]. A very high plateau is located in the middle of the TP, where the atmosphere is relatively thin. In addition, the TP is also one of the most heavily cloud-covered regions in the world, especially the southeastern part of TP, where the lack of satellite observations of TIR LST is particularly severe. Therefore, the AW LST estimation of the TP has always been a challenging task.

B. Datasets

1) FY-4A data

Fengyun-4A (FY-4A) satellite is one of China's second-generation geostationary meteorological satellites and was successfully launched on December 11, 2016. FY-4A is located in a geostationary orbit above the Equator at 104.7°E, carrying the Advanced Geostationary Radiation Imager (AGRI). AGRI has four thermal channels in 8.5–13.5 μm, which can be used to estimate LST. AGRI can perform 40 times of observations of thermal radiation emitted from the earth's surface per day with the following two observation modes: (i) the full disk (80.89°N–80.89°S, 23.5–180.00°E) observation is conducted every hour, and its start time is the full hour and the end time is 15 minutes afterward; and (ii) three consecutive full-disk observations are made at 3-hour intervals, with the observation times at **:45:00–**:59:59, **:00:00–**:14:59, and **:15:00–**:29:59. The spatial resolution of the FY-4A LST is approximately 4-km at nadir. The farther away from the nadir the observation pixels are, the lower the spatial resolution is. The specific resolution of the pixels is related to the corresponding zenith angle. The split-window algorithm proposed by Ulivieri & Cannizzaro (1985) is used to retrieve the FY-4A LST [47]. Based on the reflectance difference between clouds and the earth's surface, a threshold method is used as the cloud mask algorithm, and details for FY-4A cloud mask can be found in Xi et al. [48]. This study used the hourly FY-4A LST in 2020 and this dataset was provided by the National Satellite Meteorological Centre, China Meteorological Administration(http://satellite.nsmc.org.cn/portalsite/default.aspx).

2) Reanalysis data

The China Land Surface Data Assimilation System (CLDAS, http://data.cma.cn/data/cdcdetail/dataCode/NAFP_CLDAS2.0_NRT.html) reanalysis data from 2020 were also collected [49]–[51]. Multiple data are fused in the CLDAS, including the ground observation data, reanalysis data derived from NCEP/GFS, precipitation products, and meteorological parameters from the National Satellite Meteorological Center of China. The Space and Time Mesoscale Analysis System (STMAS), Optimal Interpolation (OI), Cumulative Distribution Function (CDF), and physical inversion are used in the production of CLDAS data [49]–[51]. In this study, the CLDAS data is mainly used to derive LST and provide meteorological elements, including air specific humidity (q), surface air temperature (T_a), and pressure (p). These CLDAS parameters have a spatial resolution of 0.0625° and a temporal resolution of 1 hour. It should be noted that FY-4A LST is not used in the generation of CLDAS LST; thus, these two LSTs are mutually independent. The quality of FY-4A and CLDAS LSTs will be evaluated in section VI-A.

3) Ground measurements

To validate the reconstructed AW LSTs, *in-situ* measurements from six ground sites with different land cover types in 2020 were collected (Table I and Fig. 1). These six ground sites, including Arou (ARO), Daman (DMA), Gaohancaodian (GHC), Yagaoshan (YGS), Huazhuaizi (HZZ), and Zhangye (ZHY), are located in the northeastern part of the TP and the surrounding areas. ARO, DMA, HZZ, and ZHY belong to the Heihe Watershed Applied Telemetry Experimental Research (HiWATER) experiment, which is a world-class observation system widely used to provide long-term and high-quality *in-situ* measurements for various satellite products validation [52]–[54]. These four sites are located in upstream and midstream of the Heihe River Basin. GHC and YGS are part of the Qilian Mountains integrated observation network [55], [56]. The land cover type of GHC is the alpine meadow, and the surface of YGS is extensively covered by alpine scrub. The *in-situ* measurements were provided by the National Tibetan Plateau Data Center (https://data.tpdc.ac.cn/en/).

These six sites provide radiation flux observations from four-component radiometers, including downward longwave radiation and upward longwave radiation. The *in-situ* LST at these sites can be calculated according to [57]:

$$T_s = \left[\frac{L_{up} - (1-\varepsilon) L_{down}}{\varepsilon \sigma} \right]^{1/4} \quad (1)$$

where T_s is the LST; L_{up} and L_{down} are the upward longwave

radiation and the downward longwave radiation, respectively; σ is the Stefan-Boltzmann constant (5.67×10^{-8} W·m^{-2}·K^{-4}); and ε is the broadband emissivity, which can be determined as follows [58]:

$$\varepsilon = 0.2122\varepsilon_{29} + 0.3859\varepsilon_{31} + 0.4029\varepsilon_{32} \quad (2)$$

where ε_{29}, ε_{31}, and ε_{32} are land surface emissivities in MODIS bands 29, 31, and 32 from MYD11A1 product (V006), respectively. The land surface emissivities under cloudy-sky conditions are obtained by linear interpolation based on clear-sky data.

In addition to longwave radiation, four sites, including ARO, DMA, GHC, and YGS, are also equipped with SI-111 TIR radiometers, which can measure the brightness temperature (BT) of the land surfaces. The BT can be further converted to LST (SI-111 LST) [59]. For these four sites, the calculated *in-situ* LSTs based on L_{up} and L_{down} have outliers. Therefore, *in-situ* LST samples are excluded when the differences between the *in-situ* LST and SI-111 LST are higher than 6 K.

The representation difference (u_{rep}) caused by the scale difference between the satellite pixel and the radiometer's field of view (FOV) is an important source of error for the validation of AW/FY-4A LST based on the *in-situ* LST. The FOVs of the site observations are much smaller (the radii are approximately 10-20 m) than those of the satellite pixels (the pixel radius is larger than 2 km), and the large-scale difference may introduce a large u_{rep}. Therefore, the effect of u_{rep} on the evaluation of FA-4A LST based on site observation should be considered as a control indicator. Here, the SRI method proposed by Ma et al. [60] is used to calculate u_{rep} between the sites and the corresponding FY-4A LST pixels. The mean u_{rep} values for the six sites are shown in Table I. A positive u_{rep} indicates a negative deviation between the estimated LST and the *in-situ* LST, and vice versa.

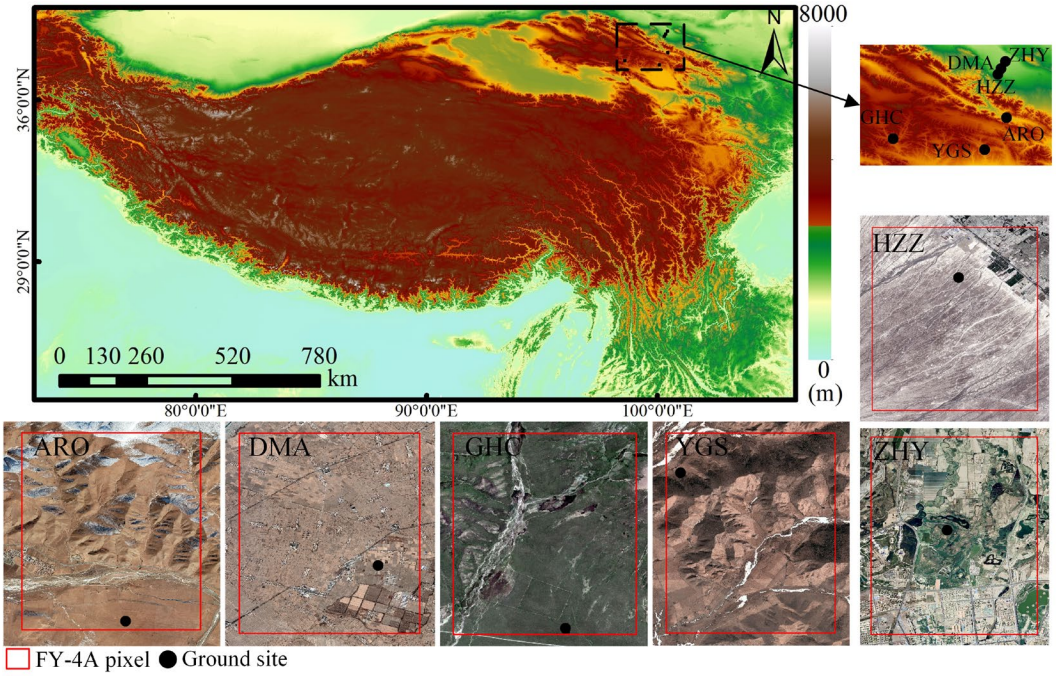

Fig. 1. DEM distribution of the study area and land cover conditions of the six selected ground sites.

TABLE I
DETAILS OF THE SIX GROUND SITES

Site	Location	Land cover	Elevation (m)	Measurement details			u_{rep} (K)
				Interval (min)	Height of radiometer (m)	Period	
ARO	100.46°E, 38.05°N	Subalpine meadow	3033	10	5	2020	-0.85
DMA	100.37°E, 38.85°N	Cropland	1556	10	12	2020	-0.09
GHC	98.59°E, 37.70°N	Alpine meadow	3718	10	6	2020	-0.35
YGS	100.10°E, 37.52°N	Alpine scrub	3495	10	6	2020	-2.32
HZZ	100.32°E, 37.77°N	Desert	1731	10	6	2020	0.43
ZHY	100.47°E, 38.98°N	Wetland	1460	10	6	2020	-3.26

Note: u_{rep} is the representation differences caused by the scale differences between satellite pixels and the radiometers' field of view (FOV).

4) Other auxiliary data

This study also uses the vegetation index and surface albedo data that are acquired by MODIS instruments on the Terra and Aqua satellites. Terra and Aqua were launched on December 18, 1999, and May 4, 2002, respectively. In this study, two categories of MODIS products in 2020 are collected, including the 16-day vegetation index product (MOD13C1) and the daily surface albedo product (MCD43C3). For MOD13C1, the normalized difference vegetation index (NDVI) with a spatial resolution of 0.05° is used in this study. The shortwave white-sky and black-sky albedos with a spatial resolution of 0.05° contained in MCD43C3 are used directly. The DEM acquired by the Shuttle Radar Topography Mission is employed in this study. The original resolution of the DEM data is 90 m. To match the spatial resolution among the FY-4A LST and these auxiliary data, the aforementioned NDVI, surface albedo, and DEM data are resampled to 0.04° through a weighted average method.

In addition, to calculate u_{rep}, Landsat-5 TM and Landsat-7 ETM+ data, GLDAS reanalysis data, and the surface emissivity products from the GLASS (Global Land Surface Satellite) products are also used. The Landsat data are used to derive the LST with a 30-m resolution and simulate the true LST within the FY-4A pixel. In this study, Landsat LST is retrieved through the radiative transfer equation method [61].

III. Methodology

A. Framework of RTG

The basis of RTG is the LST temporal decomposition theory [8], [62]. LST is decomposed into three components: the annual variation component (AVC), the diurnal variation component (ΔDVC), and the weather variation component (WVC). AVC and ΔDVC are regular varying components that only depend on time. Here, we define the sum of these two components as the normal component (NC). NC denotes the LST in the ideal state (*i.e.*, clear-sky conditions undisturbed by other factors), which is caused by the rotation and revolution of the Earth. WVC is a non-regular varying component caused by the weather and surface type, *etc.*, and it is termed as the abnormal component (AC) here. Then the AW LST from a satellite sensor can be expressed in the following form:

$$T_{\mathrm{s}}(t_{\mathrm{d}},t_{\mathrm{avg}},t)=\underbrace{\underbrace{T_{\mathrm{AVC}}(t_{\mathrm{d}},t)}_{\mathrm{AVC}}+\underbrace{[T_{\mathrm{DVC}}(t_{\mathrm{d}},t)\text{-}T_{\mathrm{DVC}}(t_{\mathrm{d}},t_{\mathrm{avg}})]}_{\Delta\mathrm{DVC}}}_{\mathrm{NC}}+\underbrace{\underbrace{T_{\mathrm{WVC}}(t_{\mathrm{d}},t)}_{\mathrm{WVC}}}_{\mathrm{AC}} \tag{3}$$

where t_{d}, t and t_{avg} are the day of year, satellite observation time and satellite average observation time, respectively; T_{AVC}, T_{DVC}, and T_{WVC} are AVC, DVC, and WVC, respectively.

The geostationary satellite has a fixed observation geometry, and its observation time t is exactly repeated each day for a given location. Therefore, t and t_{avg} in Eq. (3) are the same, and ΔDVC of NC can be neglected. Thus, Eq. (3) can be further simplified as:

$$\begin{aligned} T_{\mathrm{s}}(t_{\mathrm{d}},t)&=T_{\mathrm{AVC}}(t_{\mathrm{d}},t)+T_{\mathrm{WVC}}(t_{\mathrm{d}},t)\\ &=T_{\mathrm{NC}}(t_{\mathrm{d}},t)+T_{\mathrm{AC}}(t_{\mathrm{d}},t)\end{aligned} \tag{4}$$

where T_{NC} is NC and T_{AC} is AC.

According to Eq. (4), if the all-weather NC and AC can be determined, the AW LST based on geostationary satellites can be obtained. In RTG, we first estimate the initial NC using the annual temperature cycle (ATC) model and then fill and optimize the initial NC using the RF and the DTC model. For AC, its influencing factors are complex, and there are few physical models to express its variation. Using the FY-4A AC under clear-sky as a reference, the final AC is obtained after time correction and spatial weighting of the initial AC provided by CLDAS. The parameterization process for NC and AC is described in Sections III-B and III-C, respectively. The overall flowchart of RTG is shown in Fig. 2.

B. Determination of NC

According to Eqs. (3) and (4), NC can be determined by AVC at observation times t. AVC can be determined by ATC model [19], [63]. Thus, NC of each pixel can be expressed in the following form:

$$T_{\mathrm{NC}}(t_{\mathrm{d}},t)=T_{\mathrm{AVC}}(t_{\mathrm{d}},t)=T_{\text{NC-avg}}(t)+A_{\mathrm{NC}}\cos\left(\omega_{\mathrm{NC}}t_{\mathrm{d}}+\varphi_{\mathrm{NC}}\right) \tag{5}$$

where $T_{\text{NC-avg}}$ is the annual mean of NC; A_{NC} is the intra-annual amplitude of NC; ω_{NC} is the annual corner frequency (rad·day^{-1}), numerically $2\pi/365$ or $2\pi/366$; and φ_{NC} is the initial phase.

Next, FY-4A LST under clear-sky conditions and CLDAS LST are separately inputted into Eq. (5) to determine the corresponding coefficients:

$$\begin{cases} T_{\text{NC-F}}(t_{\mathrm{d}},t)=T_{\text{NC-avg-F}}(t)+A_{\text{NC-F}}\cos\left(\omega_{\mathrm{NC}}t_{\mathrm{d}}+\varphi_{\text{NC-F}}\right) & \text{(a)}\\ T_{\text{NC-C}}(t_{\mathrm{d}},t)=T_{\text{NC-avg-C}}(t)+A_{\text{NC-C}}\cos\left(\omega_{\mathrm{NC}}t_{\mathrm{d}}+\varphi_{\text{NC-C}}\right) & \text{(b)}\end{cases} \tag{6}$$

where the subscripts "-F" and "-C" denote FY-4A and CLDAS, respectively.

Through Eq (6a), the initial $T_{\text{NC-F}}$ can be obtained and recorded as the initial T_{NC} of AW LST. To ensure fitting accuracy, the FY-4A LST series should not be missing more than 326 days in a year. If FY-4A LST has serious missing at some moments (*i.e.*, high-temperature moments of the day), the numbers of clear-sky LST for some pixels in a year will not meet the fitting requirements of Eq. (6a). Therefore, spatially continuous T_{NC} cannot be acquired based on FY-4A LST. In addition, since there is a difference between FY-4A LST and CLDAS LST, we cannot use $T_{\text{NC-C}}$ estimated with CLDAS as the missing T_{NC}.

Fortunately, there is a strong correlation between T_{NC} and $T_{\text{NC-C}}$/other parameters. Machine learning techniques have a good ability to implicitly express the relationships between LST/LST-derived parameters and the influencing factors [61], [62]. Specifically, the RF algorithm has an excellent performance in simulating the LST variation in previous studies [56], [63], [64]. Therefore, RF is employed to estimate the missing T_{NC}. We determine the missing T_{NC} as:

$$\begin{aligned} T_{\mathrm{NC}}(t_{\mathrm{d}},t)=\mathbf{RF}_{\mathrm{NC}}(&lat,lon,DEM,NDVI,T_a,\\ &q,p,\alpha_{\mathrm{w}},\alpha_{\mathrm{b}},T_{s-C},T_{\text{NC-C}})\end{aligned} \tag{7}$$

where *lat*, *lon*, *DEM*, *NDVI*, T_{a}, q, p, α_{w}, α_{b}, $T_{s\text{-C}}$, and $T_{\text{NC-C}}$, are

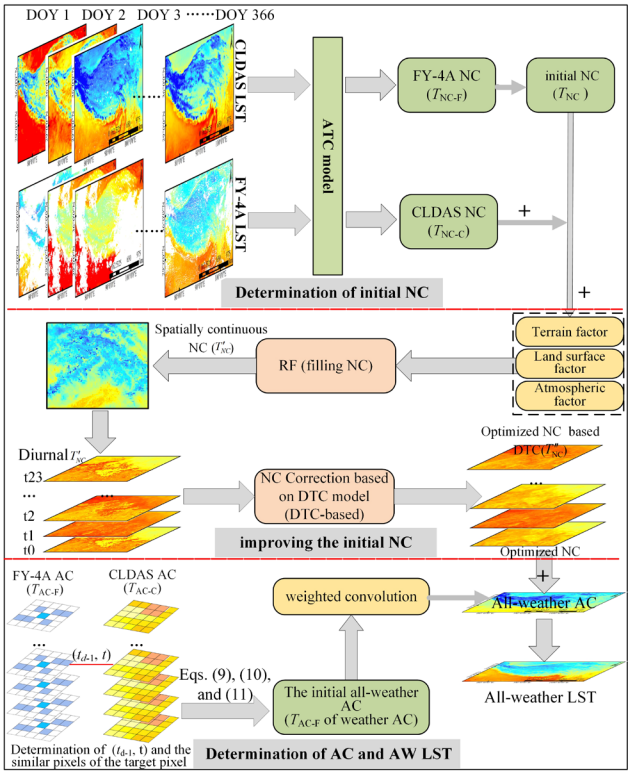

Fig. 2. Flowchart of the RTG method.

latitude, longitude, elevation, NDVI, surface air temperature, humidity, pressure, white-sky albedo, black-sky albedo, CLDAS LST, and NC of CLDAS, respectively.

First, the initial T_{NC} obtained by Eq (6a) and the possible influencing factors are imported into RF to obtain the mapping model of NC at each hour. Then the missing T_{NC} is estimated based on the RF and the possible influencing factors for obtaining spatially continuous NC (T'_{NC}).

However, due to some problems, such as the unstable data quality, uneven distribution of clear-sky LSTs on the temporal scale, and significant difference between FY-4A LST and CLDAS LST, T'_{NC} of some pixels have anomalies at some moments. Therefore, an optimization strategy is proposed to improve the initial value of T'_{NC} . In this stage, a diurnal temperature cycle-based (DTC-based) approach is employed to detect and reduce T'_{NC} anomalies. As described previously, NC represents LST in an ideal state (NC is unrelated to weather conditions). Thus, the NC values at different times during a diurnal cycle should conform to the DTC curve. When NC deviates far from the DTC curve, it should be corrected to the DTC curve. Therefore, T'_{NC} is corrected based on the DTC model from the temporal dimension. The DTC-based approach for NC optimization can be formulated as follows:

$$\begin{cases} T_{\text{NC-DTC}}(t_{\text{d}},t)=T_{\text{NC-td}}(t_{\text{d}})+ \\ \qquad A_{\text{NC}}(t_{\text{d}})\cos\left[\omega_{\text{NC-DTC}}t+\varphi_{\text{NC-DTC}}(t_{\text{d}})\right] & \text{(a)} \\ T_{\text{NC-diff-T}}(t_{\text{d}},t)=\left|T'_{\text{NC}}(t_{\text{d}},t)-T_{\text{NC-DTC}}(t_{\text{d}},t)\right| & \text{(b)} \\ T''_{\text{NC}}(t_{\text{d}},t)=T_{\text{NC-DTC}}(t_{\text{d}},t) \quad \text{if } T_{\text{NC-diff-T}}(t_{\text{d}},t)\ge T_{\text{NC-T}} & \text{(c)} \\ T''_{\text{NC}}(t_{\text{d}},t)=T'_{NC}(t_{\text{d}},t) \quad \text{if } T_{\text{NC-diff-T}}(t_{\text{d}},t)< T_{\text{NC-T}} & \text{(d)} \end{cases} \tag{8}$$

where $T_{\text{NC-DTC}}$ is the predicted NC based on the DTC model; $T_{\text{NC-td}}$ is NC at sunrise on the t_{d}-th day; t is the hour of day (for local solar time); A_{NC} is the intra-diurnal amplitude of NC; $\omega_{\text{NC-DTC}}$ is the diurnal angular frequency and is numerically equal to $2\pi/24$ and $2\pi/60$ in rad·h^{-1} during the daytime and nighttime, respectively; $\varphi_{\text{NC-DTC}}$ is the initial phase; $T_{\text{NC-diff-T}}$ is the difference between $T_{\text{NC-DTC}}$ and T'_{NC} ; T''_{NC} is the optimized NC by the DTC-based; $T_{\text{NC-T}}$ is the threshold value of $T_{\text{NC-diff-T}}$ and will be further determined.

C. *Determination of AC and AW LST*

According to Eq. (4), determining AC is essential for estimating the AW LST. AC is affected by many factors (*e.g.*, meteorological conditions and land surface characteristics) and does not follow an analytical pattern of variation [60], [64]. However, studies have shown that spatially adjacent pixels with the same land cover have similar thermal properties, provided that the land cover property does not change significantly [37]. Combining previous studies, the response of FY-4A and CLDAS to LST changes caused by meteorological parameters over a short period can be considered relatively stable (*i.e.*, the AC difference between the two LSTs at a given moment remains relatively stable over a short period) [42], [65]. The relationships between two ACs at two different hours can be parameterized in the following form.

$$\begin{cases} T_{\text{AC-F}}(t_{\text{d-1}},t)-T_{\text{AC-C}}(t_{\text{d-1}},t)=T_{\text{AC-F}}(t_{\text{d-2}},t)-T_{\text{AC-C}}(t_{\text{d-2}},t) \\ T_{\text{AC-F}}(t_{\text{d}},t)=T_{\text{s-F}}(t_{\text{d}},t)-T''_{\text{NC}}(t_{\text{d}},t) \\ T_{\text{AC-C}}(t_{\text{d}},t)=T_{\text{s-C}}(t_{\text{d}},t)-T''_{\text{NC}}(t_{\text{d}},t) \end{cases} \tag{9}$$

where the subscripts "-F" and "-C" denote FY-4A and CLDAS, respectively; $t_{\text{d-1}}$ and $t_{\text{d-2}}$ are different days of year, and $t_{\text{d-1}}$ is the reference date for $t_{\text{d-2}}$ (target day).

From Eq. (9), the following equation can be obtained:

$$\begin{cases} T_{\text{AC-F}}(t_{\text{d-2}},t)=T_{\text{AC-F}}(t_{\text{d-1}},t)+\Delta T_{\text{AC-C}} & \text{(a)} \\ \Delta T_{\text{AC-C}}=T_{\text{AC-C}}(t_{\text{d-2}},t)-T_{\text{AC-C}}(t_{\text{d-1}},t) & \text{(b)} \end{cases} \tag{10}$$

Since Eq (10) is unstable on individual pixels, we can use similar pixels in spatially adjacent pixels to build a more stable relationship. Eq (10) is further evolved into:

$$T_{\text{AC-F}}(t_{\text{d-2}},t)=T_{\text{AC-F}}(t_{\text{d-1}},t)+\sum_{i=1}^{m}w_{\text{i}}\Delta T_{\text{AC-C-i}} \tag{11}$$

where w_{i} is the weight of similar pixels.

If $t_{\text{d-1}}$ and w_{i} can be determined, $T_{\text{AC-F}}$ can be calculated at any moment. $t_{\text{d-1}}$ should satisfy the following conditions.

(1) To prevent drastic changes in land cover, the difference between $t_{\text{d-1}}$ and $t_{\text{d-2}}$ should not exceed 30 days;

(2) Target pixel at ($t_{\text{d-1}}$, t) is clear sky;

(3) On the basis of satisfying conditions 1 and 2, the date with the smallest AC difference from the target moment is selected as the reference date ($t_{\text{d-1}}$).

To identify similar pixels, the land cover was classified into four types based on NDVI: dense vegetation (NDVI≥0.5, LC-1), sparse vegetation (0.2≤NDVI<0.5, LC-2), barren ground (NDVI<0.2, LC-3), and waterbody (LC-4). The rules for determining similar pixels are as follows:

(1) Similar pixels have the same land cover as the target pixel;

(2) Similar pixels are located in a moving window centered on the target pixel. Based on the previous study, the window size is set to 11×11 pixels in this study [37], [41].

w_i can be determined as follows:

$$\begin{cases} w_i = (1/q_i)/\sum_{i=1}^{m}(1/q_i) & \text{(a)} \\ q_i = (1-r_i)\times ds_i & \text{(b)} \\ r_i = \dfrac{E[(T_{s\text{-}F\text{-}i}-E(T_{s\text{-}F\text{-}i}))(T_{s\text{-}C\text{-}i}-E(T_{s\text{-}C\text{-}i}))]}{\sqrt{D(T_{s\text{-}F\text{-}i})D(T_{s\text{-}C\text{-}i})}} & \text{(c)} \\ ds_{i0} = 1+\sqrt{(x_0-x_i)^2+(y_0-y_i)^2}/(R/2) & \text{(d)} \end{cases} \quad (12)$$

where r_i is the correlation coefficient between the FY-4A and CLDAS LSTs for the similar pixels under clear-sky conditions; ds_{i0} is the distance weight of the similar pixels (pixels as a unit of measure); (x_0, y_0) and (x_i, y_i) are the spatial location of the target pixel and similar pixels in a moving window, respectively; and R is the size of the moving window.

In the process of AC estimation, the change information of AC comes from CLDAS. However, there is some uncertainty in CLDAS, and some pixels cannot satisfy the estimation conditions of AC at some moments. Thus, it is necessary to further fill and optimize the initial AC obtained based on Eq (11). In this process, a weighted convolution method based on a moving window (the window size remains the same as before) is used. A similar approach has been used in previous studies [37]. Previous studies have shown that AC varies minimally over small spatial scales [37]. After the negative systematic bias is eliminated, the optimized AC in a target pixel can be expressed as a weighted sum of reference pixels within the moving window. The referenced pixel belongs to the same land cover and weather conditions (clear sky or cloudy sky) as the target pixel. If the target pixel already has an AC value, it will be aligned with the referenced pixel.The optimized AC in target pixel can be expressed as:

$$T_{AC}(t_d,t)=\begin{cases} \text{if } T_{AC\text{-}F\text{-}tar} \text{ does not exist:} \\ \sum_{m=1}^{N} T_{AC\text{-}F\text{-}m}(t_d,t)\cdot W_m & \text{(a)} \\ \text{if } T_{AC\text{-}F\text{-}tar} \text{ exist:} \\ \sum_{m=1}^{N}[T_{AC\text{-}F\text{-}m}(t_d,t)\cdot W_m \cdot \dfrac{N}{N+1} \\ +T_{AC\text{-}F\text{-}tar}(t_d,t)\cdot \dfrac{1}{N+1}] & \text{(b)} \end{cases} \quad (13)$$

where T_{AC} is the all-weather AC; N is the number of referenced pixels; W_m is the weight of referenced pixels, and it is determined as follows:

$$W_m = \frac{1/ds_m}{\sum_{r=1}^{N}(1/ds_m)} \quad (14)$$

where ds_m is the distance between the target and reference pixels, which can be determined by Eq (12d).

After obtaining the optimized all-weather NC and AC, the reconstructed AW LST can be obtained:

$$T_{s\text{-}AW}(t_d,t) = T''_{NC}(t_d,t) + T_{AC}(t_d,t) \quad (15)$$

where $T_{s\text{-}AW}$ is the reconstructed AW LST.

D. Implementation of RTG

The proposed RTG can be implemented using the following eight steps.

Step I: The spatial and temporal extents of all relevant data are unified. All datasets are resampled to a 0.04° grid using a weighted average method.

Step II: The FY-4A LST and CLDAS LST in Step I are substituted into Eq (5) to obtain the NC parameters (pixel-by-pixel implementation). After the fitting is completed, NCs of FY-4A and CLDAS are calculated separately based on Eq. (6). Based on the results of the follow-up evaluation, FY-4A LST is considered as better data with lower uncertainty. Therefore, $T_{NC\text{-}F}$ is used as the initial NC for the all-weather LST (T_{NC}).

Step III: Based on Eq (7), T_{NC} in step 2 is used as the label, and $T_{NC\text{-}C}$ and other influencing factors are regarded as features. Then, the RF model is trained for NC estimation in space (NC estimation models are developed based on the entire study area). Later on, the trained RF model is used to estimate the spatially continuous all-weather NC (T'_{NC}).

Step IV: The DTC-based approach is applied to optimize T'_{NC} (Eq. 8). First, T'_{NC} from Step III is substituted into Eq. (8a) to obtain the relevant parameters (*i.e.*, $T_{NC\text{-}td}$, A_{NC}, and $\varphi_{NC\text{-}DTC}$). Second, $T_{NC\text{-}DTC}$ is estimated based on Eq. (8a). Third, T'_{NC} and $T_{NC\text{-}DTC}$ are substituted into Eq. (8b) to calculate $T_{NC\text{-}diff\text{-}T}$. Ideally, $T_{NC\text{-}diff\text{-}T}$ should be 0, but the uncertainty of the input data can lead to a bias in $T_{NC\text{-}diff\text{-}T}$. Thus, we set the threshold value ($T_{NC\text{-}T}$) of the $T_{NC\text{-}diff\text{-}T}$ to 2.5 K (about three times the standard deviation of the mean $T_{NC\text{-}diff\text{-}T}$ of the normal region) and correct the NC according to Eq. (8c) and Eq. (8d). Finally, we obtain the optimized NC (termed T''_{NC}), which will be used eventually to calculate the AW LST.

Step V: The estimation of AC. The study area is divided into four land covers (dense vegetation, sparse vegetation, barren ground, and waterbody) according to NDVI levels. After determining the referenced date $t_{d\text{-}1}$ and the weights of similar pixels at the target moment according to the rules in the moving window, the initial all-weather AC is finally calculated based on Eqs (9), (10), (11), and (12).

Step VI: The filling and optimization of initial AC. Under the assumption that neighboring pixels with the same weather conditions have small AC variations, we perform AC convolution operation according to Eqs. (13) and (14) in the moving window of step V for filling and optimizing the initial AC.

Step VII: After step VI has been looped 3 times, the last missing NC is filled using the mean AC within the moving window to obtain a spatially contiguous AC (T_{AC}).

Step VIII: T''_{NC} and T_{AC} obtained in Step IV and Step VII are summed (Eq. 15) to obtain the AW LST.

IV. Results and Discussion

A. Evaluation of the input datasets

1) Statistics of FY-4A LST missing pixels

To grasp the missing FY-4A LST at different hours, the number of missing days of FY-4A LST over the TP was counted. The spatial distribution of the missing FY-4A LST in 2020 is shown in Fig. 3. After comparing the missing rate of FY-4A LST in the daytime (07:00 - 16:00, if not specified, all times are local solar time at the longitude of 90°E) and nighttime (17:00 - 06:00), an unsurprising result is found that the FY-4A LST images in the daytime lack more valid values than that of nighttime, especially in the central part of the TP. The possible reason for this phenomenon is that the land surface has stronger evaporation during the daytime, thus causing more evident cloud coverage. In terms of spatial distribution, the region with the highest missing rate is the southeastern part of the TP, with the missing day up to 300 days. In contrast, the missing LST in the northwestern part of the TP is relatively less than that in the southeastern part. Furthermore, we also calculated the mean value and standard deviation (STD) for the missing days at the 24 hours (see Fig. 4). From the mean value of missing days (see Fig. 4a), the TP has a large number of missing data at all hours, with a missing rate of more than 1/3. In contrast, the STD of missing days (see Fig. 4b) is relatively small, and the STD values in most regions are less than 50 days, suggesting that the missing of FY-4A LST pixels is a frequent event in the TP. Because the vast majority of missing data are caused by clouds, it is necessary and urgent to estimate the cloudy-sky LST based on FY-4A data for obtaining the AW LSTs.

2) Validation of FY-4A and CLDAS LST

Since this study aims to estimate the AW LST using the FY-4A LST and CLDAS data, the accuracies of the FY-4A and CLDAS LSTs need to be validated before conducting the study. Based on the *in-situ* LSTs in the TP, the evaluation results of FY-4A and CLDAS LSTs are shown in Table II. Before the evaluation, the LST outliers are removed with the 3σ (standard deviations) filtering [66], [67].

Table II indicates that FY-4A LST outperforms CLDAS LST. The RMSE differences between FY-4A LST and CLDAS LST are 0.69 K (ARO), 2.27 K (DMA), 2.71 K (GHC), 1.42 K (YGS), 1.97 K (HZZ), and 1.21 K (ZHY), respectively. For FY-4A LST, LSTs at DMA, GHC, and HZZ perform better, while LSTs at ARO, YGS, and ZHY have lower accuracy. One possible reason for this phenomenon is that DMA, GHC, and HZZ have better spatial representativeness with a u_{rep} of -0.09 K, -0.34 K, and 0.43 K (Table I), respectively. In contrast, ARO, YGS, and ZHY have poorer spatial representativeness, with a

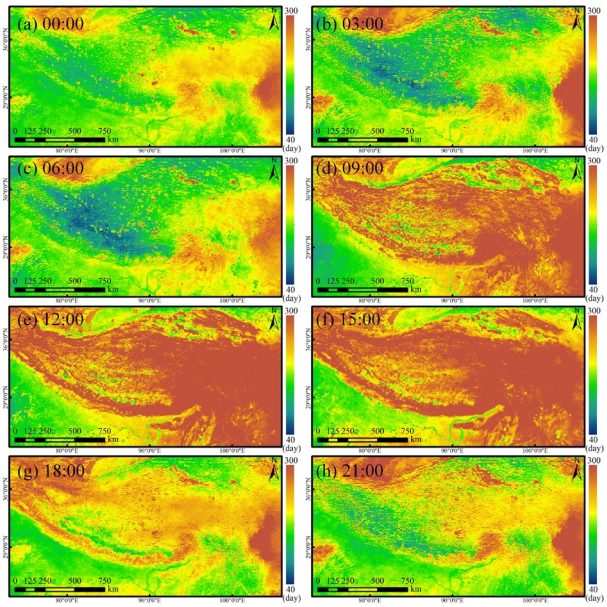

Fig. 3. Statistical results of the missing days for FY-4A LST at different hours in 2020. The time is the local solar time at the longitude of 90°E.

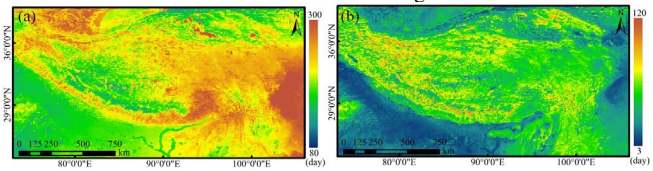

Fig. 4. Mean value and standard deviation (STD) for the missing days at the 24 observation times. (a) Mean value; (b) STD.

TABLE II
Validation Results of FY-4A and CLDAS LSTs under Clear-Sky Conditions

Site	FY-4A				CLDAS			
	RMSE (K)	MBE (K)	R^2	N	RMSE (K)	MBE (K)	R^2	N
ARO	4.32	-1.77	0.92	3890	5.01	2.03	0.89	3890
DMA	3.13	-1.34	0.96	4004	5.40	1.95	0.89	4004
GHC	3.35	-1.26	0.96	1899	6.06	1.80	0.85	1899
YGS	4.84	1.31	0.88	3901	6.16	3.75	0.90	3901
HZZ	3.68	-1.31	0.95	4487	5.65	2.24	0.89	4487
ZHY	4.98	-0.77	0.89	4837	6.19	2.30	0.93	4837

u_{rep} of -0.85 K, -2.32 K, and -3.26 K, respectively (Table I). After considering u_{rep} (MBE_{new} = MBE + u_{rep}), all six sites showed various systematic biases of MBE_{new} with -2.62 K (ARO), -1.43 K (DMA), -1.6 K (GHC), -1.01 K (YGS), -0.88 K (HZZ), and -4.03 (ZHY), respectively. For CLDAS LST, RMSEs of the six sites are 5.01 K (ARO), 5.40 K (DMA), 6.06 K (GHC), 6.16 K (YGS), 5.65 K (HZZ), and 6.19 K (ZHY), respectively. In addition, there is an obvious overestimation phenomenon for MBEs of six sites, with 2.03 K (ARO), 1.95 K (DMA), 1.80 K (GHC), 3.75 K (YGS), 2.24 K (HZZ), and 2.30 K (ZHY), respectively. The possible reasons for the underestimation of FY-4A LST are the impact of cloud contamination. Meanwhile, the larger satellite observed zenith angle also introduces the underestimation of LST. For the overestimation of CLDAS, the possible reasons are mainly the

input data or the assimilation algorithm.

In addition, we also selected valid FY-4A LST and CLDAS LST for 24 hours of DOY 90, 180, 270, and 360 in 2020 to perform the intercomparison between the two types of LST (Fig. 5). Fig. 5 shows a significant overestimation of CLDAS compared to the FY-4A, with an MBE range from 3.35 K to 5.44 K. The difference between these two LSTs is significant, with RMSEs above 7 K. According to the previous validation results, the accuracy of FY-4A LST is higher than that of CLDAS LST, and the estimated AW-LST is an FY-4A-like LST, whose final estimation accuracy depends on the original FY-4A LST and CLDAS LST.

B. The estimated NC and AC

1) Initial NC

Based on Eqs. (5) and (6), it can be noted that the initial NC (T_{NC}) estimation is mainly performed by using FY-4A LST. To illustrate the reasonableness of NC estimation based on the RTG, we first test the NC estimation for the corresponding FY-4A LST at six sites. Fig. 6 shows a test result at 06:00 in 2020 with *in-situ* LST.

Fig. 6 shows that the *in-situ* NC can be fitted by the annual temperature cycle (ATC) model based on *in-situ* LST. On DOY 250 - 300, although many missing *in-situ* LSTs exist at GHC, the *in-situ* NC curves still reflect the intra-annual variation of LST, with an RMSE of 3.87 K between *in-situ* LST and *in-situ* NC. For all six sites, *in-situ* LSTs present slight fluctuation and are mainly concentrated around the NC curve (the RMSEs between *in-situ* NC and LST range from 2.43 K - 3.98 K), indicating the annual trend of NC is obvious.

NC (T_{NC}) calculated from FY-4A LST has excellent agreement with the corresponding FY-4A LST (LST RMSEs vary from 2.59 K - 2.96 K). This finding indicates that it is reasonable and feasible to fit T_{NC} based on FY-4A LST. The difference between T_{NC} and FY-4A LST (mean RMSE is 2.80 K) is smaller than the difference between the *in-situ* NC and *in-situ* LST（mean RMSE is 3.41 K). The difference between NC and LST is caused by AC. AC is directly related to weather conditions. Therefore, one reason for this phenomenon may be that the meteorological parameters have fewer influences on LST at the pixel scale than that of the site scale. In addition, despite the scale differences between the *in-situ* NC and T_{NC} are large, both two NCs are highly similar for the six sites in terms of various trends (the highest NC appeared at the same time). The test results indicate that the ATC-based model is effective in fitting T_{NC} and can be used for pixel-by-pixel T_{NC} simulations.

With the same procedure in Step II (Section III-D), we further estimated T_{NC} for the entire TP in 2020. T_{NC} at 06:00 and 12:00 on DOYs 061, 121, and 241 in 2020 are shown in Fig. 7. Obviously, the spatial distribution of T_{NC} is consistent with the priori knowledge of the LST distribution on the TP. In the southeastern part of the TP, T_{NC} with a 0.04° resolution can better reflect the geographic variation of LST, which is more evident at 06:00. For the intra-annual variation, T_{NC} has an obvious trend, and this is because the characteristics of T_{NC} are related to the earth's rotation. According to the previous

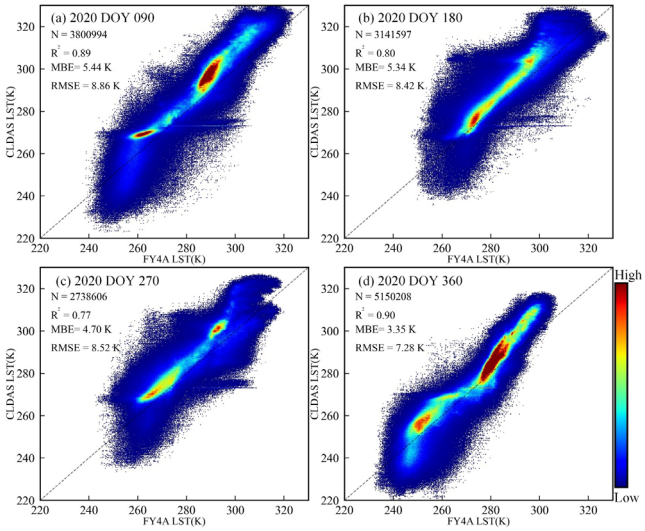

Fig. 5. Density plots between the FY-4A LST and CLDAS LST on DOY 90, 180, 270, and 360 in 2020.

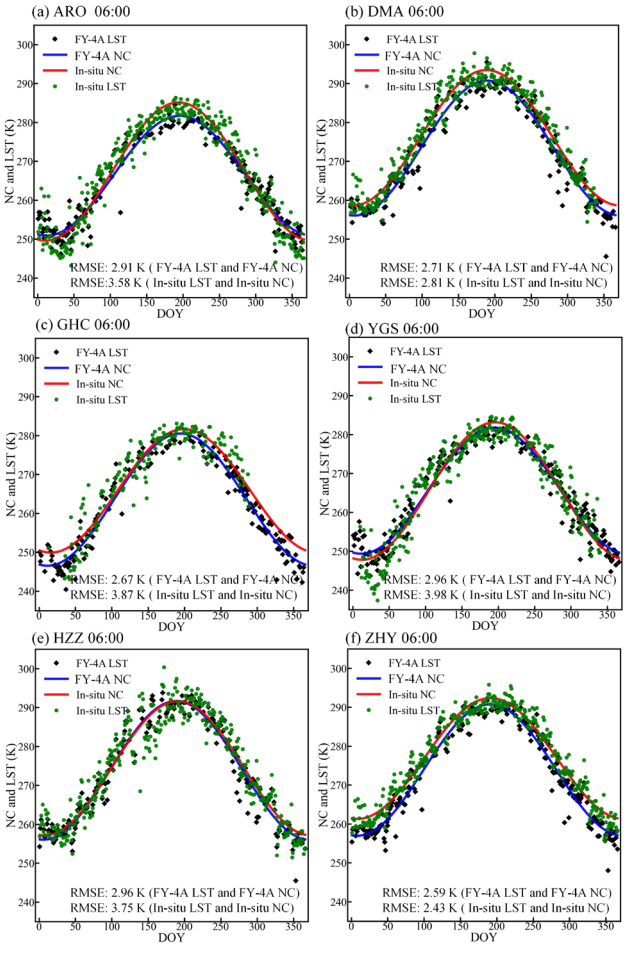

Fig. 6. The test results of NC fitting for the six sites. The time is the local solar time at the longitude of 90°E.

analysis, FY-4A LST has many missing data at some hours and in some regions, and the FY-4A LST series are not uniformly distributed in an intra-annual cycle. These problems will contribute to the failure of T_{NC} estimation. We can see that T_{NC} has different degrees of missing at various hours. Especially at 12:00, its spatial missing is more obvious. Therefore, T_{NC} needs to be further filled and optimized before using it as the input

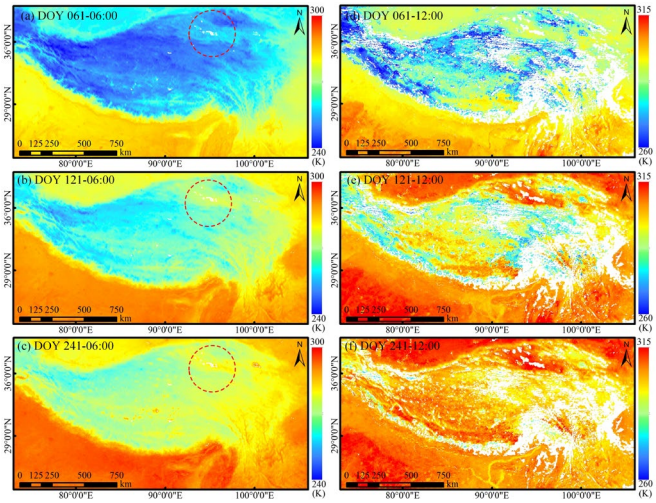

Fig. 7. The spatial distribution of the initial T_{NC}. (a), (b), and (c): nighttime; (d), (e), and (f): daytime. The time is the local solar time at the longitude of 90°E.

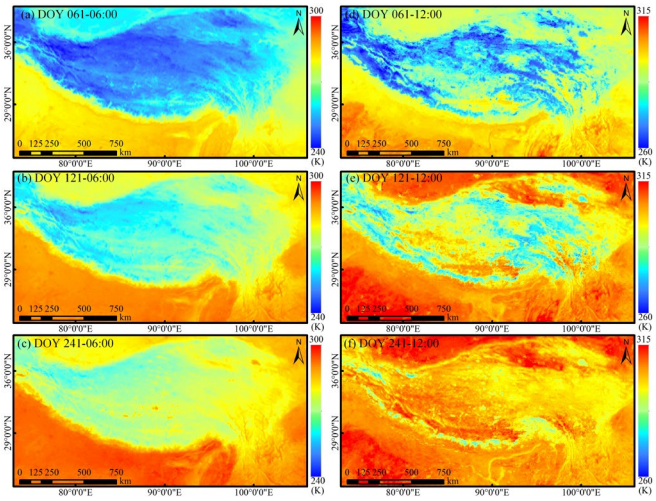

Fig. 8. The optimization results of the initial NC. (a), (b), and (c): nighttime; (d), (e), and (f): daytime.The time is the local solar time at the longitude of 90°E.

data to calculate the AW LST.

2) Optimization of NC

Since T_{NC} has some missing values (Fig. 7), RF is first used to fill the spatial missing of T_{NC} to obtain the spatially continuous NC (T'_{NC}). This process is implemented as described in Step III of Section III-D. Then, to further remove the anomalies that occur at some pixels in T'_{NC} , a DTC-based approach is proposed to obtain the final NC (T''_{NC}) based on the characteristics of geostationary satellites with a high-frequency observation (here, it is defined as time optimization). The temporal optimization is implemented as described in Step VI of Section III-D. The core theory of time optimization is that T'_{NC} is LST in the ideal state; thus, T'_{NC} should conform to the DTC model during the day. If T'_{NC} deviates from the DTC curve at a certain moment and exceeds a threshold, we believe that T'_{NC} needs to be corrected to the DTC curve.

The final NC (T''_{NC}) at 06:00 and 12:00 on DOYs 061, 121, and 241 in 2020 are shown in Fig. 8. Comparing to Fig. 7, it is evident that before the filling, NC has lots of missing values, especially at 12:00. After the filling, all missing NCs are successfully estimated, and a spatially continuous NC is obtained, indicating that RF can effectively estimate the missing NC in small regions. In addition, spatial anomalies of NC can be effectively suppressed by time optimization, and there are no obvious NC anomalies in Fig. 8. The lower temperatures occur at nighttime when the spatial distribution of LST is homogeneous. The mean image gradients (which characterize the roughness of the LST in space) for the two moments are calculated, and the mean gradients are 0.59 K and 1.44 K for 06:00 and 12:00, respectively. Comparing T''_{NC} at 06:00 (nighttime) and 12:00 (daytime), we find that T''_{NC} at 06:00 is smoother in the spatial distribution, with weaker spatial variation in a small area and natural visual perception. Compared to T''_{NC} at 06:00, T''_{NC} at 12:00 is more complex in the spatial distribution, with some obvious regional variations and rougher visual perception. At high-temperature moments (the hours having larger LSTs of the day), NC is affected by solar radiation, and there are some regional differences. Winter has a larger solar zenith angle, and LST is less affected by the sun. Therefore, T''_{NC} at 12:00 on DOY 061 is smoother than T''_{NC} on DOY 121, which indirectly confirms this inference. Overall, the image's visual effect is consistent with the gradient calculation results. T''_{NC} can be obtained to calculate the AW LST.

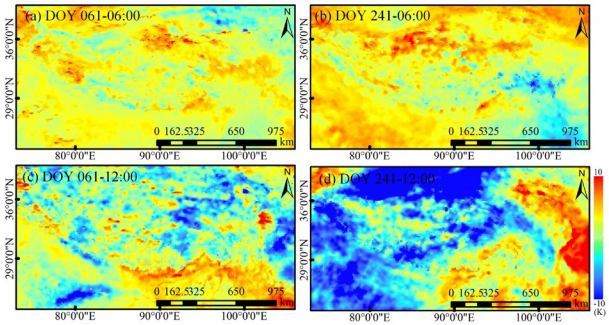

Fig. 9. Spatial pattern of the all-weather AC for the TP. The time is the local solar time at the longitude of 90°E.

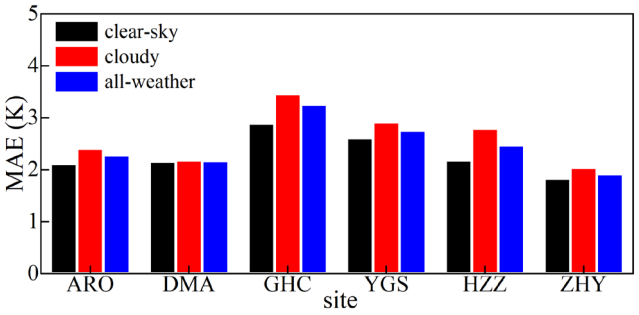

Fig. 10. The validation results of estimated all-weather AC based on the in-situ AC.

3) The estimated AC

AC is estimated according to Steps V, VI, and VII in Section III-D. The FY-4A LST is severely missing at some pixels within a year. In addition, the uncertainty of the input data may

TABLE III
VALIDATION RESULTS OF AW LST AND CLDAS LST UNDER CLEAR-SKY (CLOUDY-SKY), DAYTIME (NIGHTTIME), AND ALL-WEATHER (ALL-TIME) CONDITIONS

Site	LST	Clear-sky (Cloudy-sky)				Daytime (Nighttime)				All-weather (All-time)			
		RMSE (K)	MBE (K)	R^2	N	RMSE (K)	MBE (K)	R^2	N	RMSE (K)	MBE (K)	R^2	N
ARO	AW	**2.74** (**4.22**)	-0.58 (-2.76)	0.97 (0.93)	3889 (4724)	**3.79** (**3.49**)	-1.81 (-1.75)	0.93 (0.94)	3569 (5044)	**3.62**	-1.78	0.95	8613
	CLDAS	5.01 (4.49)	2.03 (-0.27)	0.89 (0.86)	3889 (4274)	5.01 (4.55)	-1.64 (2.81)	0.85 (0.89)	3569 (5044)	4.75	0.97	0.88	8613
DMA	AW	**2.37** (**3.73**)	-0.21 (-1.85)	0.97 (0.93)	4004 (4028)	**3.25** (**3.02**)	0.09 (-1.84)	0.93 (0.96)	3369 (4663)	**3.12**	-1.03	0.95	8032
	CLDAS	5.40 (4.61)	1.95 (1.14)	0.89 (0.89)	4004 (4028)	6.22 (3.77)	1.62 (1.15)	0.84 (0.90)	3369 (4663)	4.95	1.35	0.89	8032
GHC	AW	**2.73** (**4.31**)	0.14 (-1.01)	0.96 (0.90)	1891 (3318)	**4.22** (**3.49**)	0.52 (-1.35)	0.87 (0.92)	2114 (3095)	**3.81**	-0.59	0.92	5209
	CLDAS	6.06 (4.68)	1.80 (0.35)	0.85 (0.85)	1891 (3318)	5.84 (3.94)	-1.03 (1.84)	0.78 (0.90)	2114 (3095)	4.81	0.68	0.87	5209
YGS	AW	**3.12** (**3.71**)	0.97 (-0.81)	0.94 (0.90)	3868 (4026)	**3.86** (**3.08**)	1.56 (-1.01)	0.90 (0.94)	3307 (4587)	**3.43**	0.06	0.93	7894
	CLDAS	6.16 (3.49)	3.75 (-0.66)	0.90 (0.90)	3868 (4026)	3.77 (4.02)	-1.42 (2.17)	0.91 (0.90)	3307 (4587)	4.01	0.67	0.92	7894
HZZ	AW	**2.71** (**3.52**)	0.05 (-0.80)	0.97 (0.95)	4487 (4007)	**3.70** (**2.62**)	-0.75 (-0.07)	0.95 (0.95)	3533 (4961)	**3.12**	-0.35	0.96	8494
	CLDAS	5.65 (4.74)	2.24 (2.29)	0.89 (0.92)	4487 (4007)	5.07 (5.34)	0.19 (3.74)	0.90 (0.91)	3533 (4961)	5.23	2.27	0.91	8494
ZHY	AW	**4.45** (**4.18**)	0.48 (-0.28)	0.92 (0.90)	4837 (3806)	**5.54** (**3.18**)	3.74 (-2.42)	0.91 (0.97)	3596 (5047)	**4.33**	0.14	0.92	8643
	CLDAS	6.19 (6.45)	2.30 (3.68)	0.93 (0.93)	4837 (3806)	8.45 (4.01)	5.99 (0.71)	0.94 (0.92)	3596 (5047)	6.26	2.91	0.93	8643

cause anomalies in the initial AC of a small number of pixels. By filling and optimizing the AC, we obtained all-weather AC (T_{AC}).

Fig. 9 displays the estimation results of T_{AC} at 06:00 and 12:00 on DOY 061 and 241. Although T_{AC} is estimated pixel-by-pixel, there are no significant spatial anomalies for the entire TP. This finding indicates that the proposed AC estimation method is stable and generalizable. T_{AC} is present in both positive and negative values, showing that LST has an obvious spatial variation. A closer look indicates large variation in some regions at some moments (with varying amplitude reaching 10 K). Thus, the estimated T_{AC} can be used for AW LST estimation.

The *in-situ* ACs at six sites are extracted to validate the estimated T_{AC} by RTG. The calculated mean absolute error (MAE) between *in-situ* AC and T_{AC} is shown in Fig. 10. For the clear-sky condition, the MAE ranges from 1.83 K (ZHY) to 2.89 K (GHC). For the cloudy-sky conditions, the MAE ranges from 2.04 K (ZHY) to 3.46 K (GHC). Overall, the MAE under clear-sky conditions is lower than that under cloudy-sky conditions. The possible reason for this phenomenon is that the weather conditions are more complex under cloudy-sky conditions than clear-sky conditions. For the all-weather condition, the MAE ranges from 1.92 K (ZHY) to 3.26 K (GHC). The large differences between the estimated T_{AC} and the *in-situ* AC are found at some sites. The possible reason for this phenomenon is that there is a scale difference between sites and pixels, and the *in-situ* AC is more susceptible to the weather compared to the T_{AC} at the pixel. In addition, according to Eq (4), the accuracy of the final AW LST is also related to NC in addition to AC. Therefore, the difference between the *in-situ* AC and the T_{AC} at pixel scale does not ultimately determine the accuracy of AW LST. The predicted T_{AC} has stable accuracies, with a mean MAE of 2.48 K at all six sites. The results indicate that the proposed method can effectively estimate the AC, which can be used to estimate the all-weather AC (T_{AC}) over TP.

C. The reconstructed AW LST

1) Validation against the in-situ LST

To quantitatively evaluate the accuracy of RTG, the reconstructed AW LSTs under clear-sky, cloudy-sky, and all-weather conditions are validated against the *in-situ* LST. Table III presents the validation results of RTG at various weather conditions for the six ground sites. As a control, the validation results of CLDAS LST under three weather conditions are also presented in Table III.

Table III clearly shows that the reconstructed AW LST with RTG has better accuracy (mean RMSE is 3.02 K) for the clear-sky condition than FY-4A and CLDAS LSTs. For AW LST, the RMSEs/MBEs are 2.74 K/-0.58 K (ARO), 2.37 K/-0.21 K (DMA), 2.73 K/-0.14 K (GHC), 3.12 K/0.97 K (YGS), 2.71 K/0.05 K (HZZ), and 4.45 K/0.48 K (ZHY), respectively. The systematic deviations for all six sites are within 1 K. Compared to the FY-4A LST (Table II), the original underestimation is significantly depressed in reconstructing the AW LST. For all six sites, the RMSE of the AW LST is lower than that of the FY-4A LST. The RMSEs of FY-4A LST can be reduced by 1.58 K (ARO), 0.76 K (DMA), 0.62 K (GHC), 1.72 K (YGS), 0.97 K (HZZ), and 0.54 K (ZHY), respectively (Table II). Compared to the CLDAS LST, the original overestimation effect is significantly depressed in reconstructing the AW LST. The RMSEs of CLDAS LST can be reduced by 2.27 K (ARO), 2.03 K (DMA), 3.33 K (GHC), 3.04 K (YGS), 2.94 K (HZZ), and 1.74 K (ZHY), respectively. R^2 between the reconstructed AW LST and *in-situ* LST are all greater than 0.9 for all six sites, indicating the reconstructed AW LSTs with RTG have a good agreement with *in-situ* LST under clear-sky conditions. The

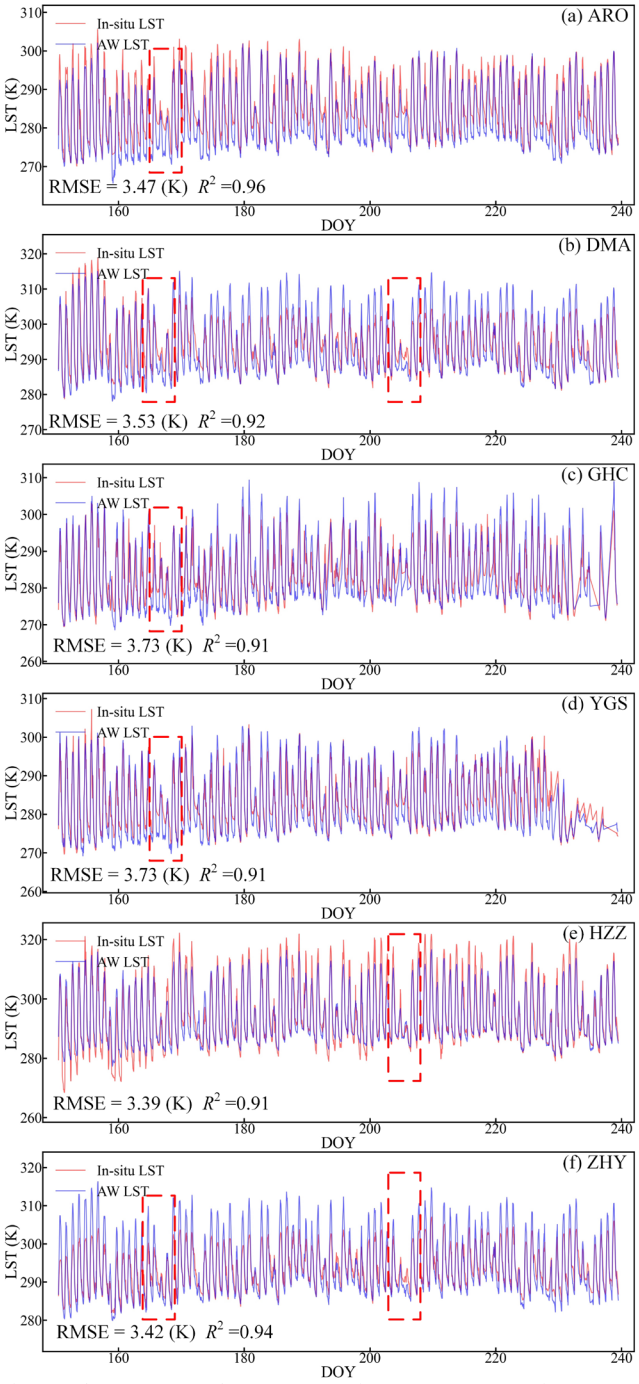

Fig. 11. The AW LST and *in-situ* LST series on DOY 150-240 in 2020.

validation results under clear-sky conditions show that RTG can significantly improve the systematic bias and increase the accuracy of the input data (*i.e.*, FY-4A LST and CLDAS LST).

The accuracy of AW LST under cloudy-sky conditions is slightly lower than that of clear-sky conditions, with a mean RMSE of 3.94 K. For the six sites, the RMSEs/MBEs are 4.22 K/-2.76 K (ARO), 3.73 K/-1.85 K (DMA), 4.31 K/-1.01 K (GHC), 3.71 K/-0.81 K (YGS), 3.52 K/-0.80 K (HZZ), and 4.18 K/-0.28 K (ZHY), respectively. Negative systematic errors can be found, indicating the reconstructed AW LSTs have an underestimation under cloudy-sky conditions. In addition, according to Eq (11), we know that the AC under cloudy-sky conditions is related to the AC of FY-4A under the clear-sky status. Therefore, the underestimation of AW LST under cloudy-sky conditions is related to the underestimation of FY-4A LST under clear-sky conditions. AW LST has better accuracy than CLDAS LST. Except for the YGS site, the RMSEs of CLDAS LST are reduced by 0.25 K (ARO), 0.88 K (DMA), 0.37 K (GHC), 1.22 K (HZZ), and 2.27 K (ZHY), respectively. R^2 between AW LST and *in-situ* LST is higher than 0.9 under cloudy-sky conditions, indicating the reconstructed AW LSTs with RTG have a good agreement with *in-situ* LSTs under cloudy-sky conditions. The validation results show that RTG can better estimate the LST under cloudy-sky conditions, but its accuracy is affected by the uncertainty of input data.

The mean RMSEs of AW LST and CLDAS are 3.57 K and 5.53 K, respectively, under all-weather conditions. After the CLDAS LST is fused by RTG, its RMSEs are reduced by 1.13 K (ARO), 1.83 K (DMA), 1.0 K (GHC), 0.58 K (YGS), 2.11 K (HZZ), and 1.93 K (ZHY), respectively, under the all-weather conditions. The AW LST for all six sites has a high agreement with the *in-situ* LST under all-weather conditions, with R^2 values above 0.91. For the ZHY site, the accuracy of AW LST is lower than the other five sites under three weather conditions. Through a closer look at Fig. 1, one can be found that the FY-4A pixel at ZHY is mainly composed of the urban area (with a large number of buildings), which can lead to a large difference between the LST at pixel scale and the *in-situ* LST (u_{rep} = -3.26). In contrast, the AW LSTs at the other five sites also have good accuracy. However, there is still a significant systematic bias for some sites, mainly caused by underestimating the AW LST under cloudy-sky conditions. The site-based validation results show that RTG can better estimate AW LSTs based on FY-4A and CLDAS LST under clear-sky, cloudy-sky, and all-weather conditions. In particular, RTG can significantly improve the accuracy of the original input data at clear-sky conditions.

The accuracies of AW LST and CLDAS LST in the daytime (07:00-16:00) and nighttime (17:00-06:00) are also evaluated (Table III). Overall, the AW LST has better accuracy at nighttime than daytime, and a similar case is found for CLDAS LST. The mean RMSEs of AW (CLDAS) LST during daytime and nighttime are 4.06 K (5.73 K) and 3.1 K (4.28 K), respectively. There are three possible reasons for this phenomenon. First, LST has better spatial homogeneity at night. Second, FY-4A LST has a higher percentage of clear sky at nighttime than daytime, which is more beneficial for RTG execution at nighttime. Third, CLDAS LST, as one of the data, has better accuracy at night. The accuracy difference of the reconstructed AW LST by the RTG method between the daytime and nighttime is less than 1 K, indicating that the RTG method has strong applicability in both daytime and nighttime.

2) Time series evaluation

To further evaluate the performance of the proposed RTG method in terms of time series, the AW LST and *in-situ* LST series on DOY 150-240 in 2020 are shown in Fig.11. For comparing the time series change of AW LST clearly, Fig.11 merely shows the LST series from DOY 150 to DOY 240.

It can be found that AW LST has a good agreement with the

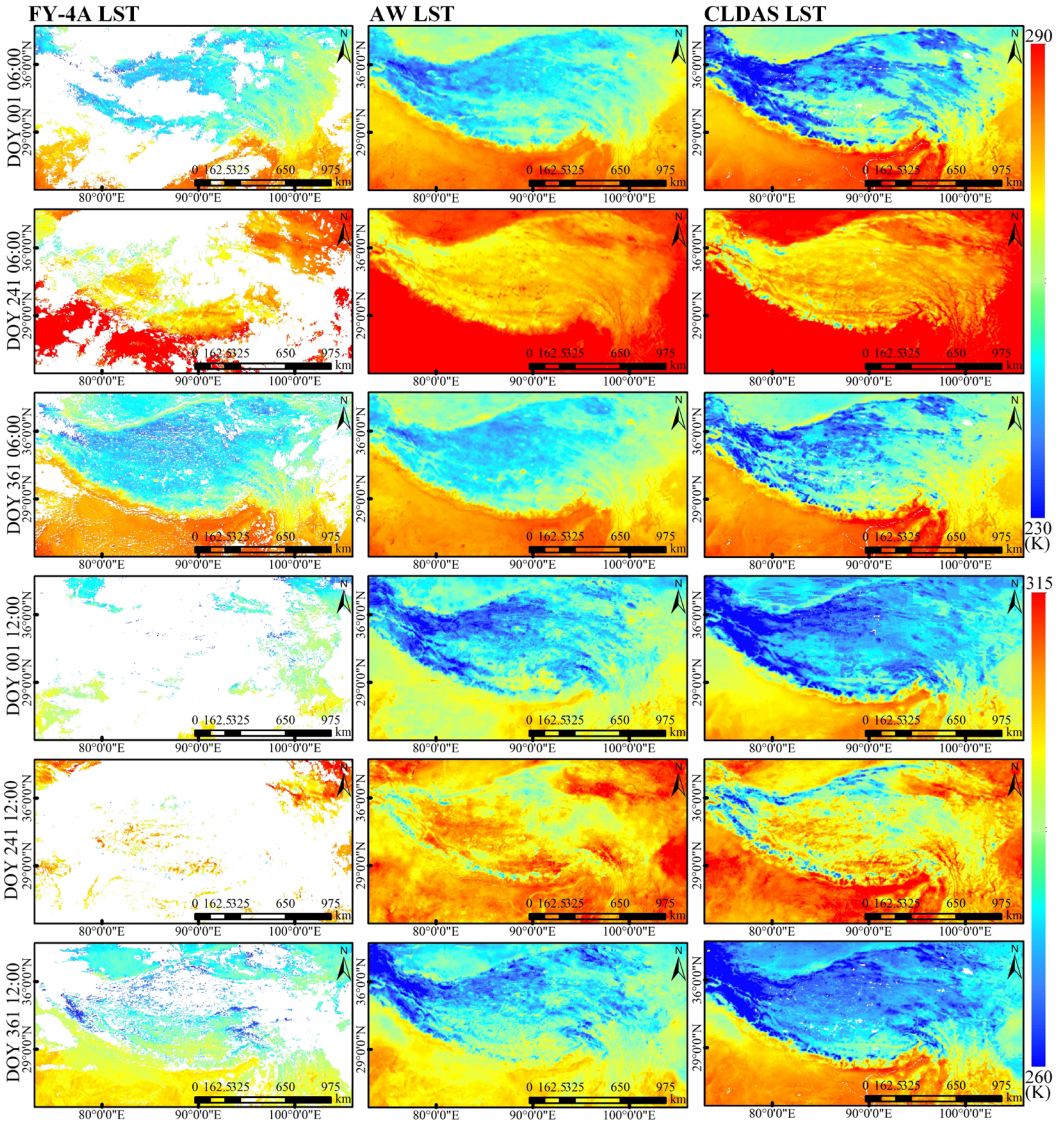

Fig. 12. Spatial pattern of the FY-4A LST, AW LST, and CLDAS LST for the TP at 06:00 and 12:00 on DOY 121, 241, and 361 in 2020. The time is the local solar time at the longitude of 90°E.

in-situ LST during DOY 150-240, with R^2 values above 0.91. However, for some sites, there are significant differences between the highest/lowest values of AW LSTs and *in-situ* LSTs during the day. There are two possible reasons for this phenomenon. The first one is the deficiency of RTG in capturing the maximum and minimum values of LST during the day. The second one is that there is a scale mismatch between the sites and the corresponding pixels, leading to the difference being significantly magnified at the high/low temperature moments of a day. For example, the land cover type of the ZHY site is the wetland, while the corresponding FY-4A pixel contains many urban areas. There is a significant heat island effect in urban areas during the highest temperature moments of the day, which leads to higher LST values for pixels. This could well explain why the AW LST is higher than the *in-situ* LSTs during the highest temperature moments of the day. In addition, the AW LST is highly consistent with the *in-situ* LST at other moments of the day except for the moments of high/low LST. All six sites have stable accuracy during DOY 150-240, with RMSEs varying from 3.39 K to 3.73 K. A closer look at Fig. 11 reveals that the AW LST is able to maintain synchronous changes with the *in-situ* LST when the LST is mutated at certain dates (these dates are marked by the red rectangular box in Fig. 11).

3) Spatial patterns of AW LST

To further examine the spatial distributions of AW LST, Fig. 12 lists some examples of reconstructed AW LST and CLDAS LST, and the original FY-4A LST is also given. For the selected examples, the continuous cloudy-sky conditions mainly appear in the southeastern part of the TP for both daytime and nighttime, as shown by the FY-4A LST. After the AW LSTs are reconstructed with the RTG method, the missing FY-4A LSTs at cloudy-sky conditions are effectively filled.

To reduce the underestimation issue of FY-4A LST in some regions, we used the clear-sky LST determined by the RTG method instead of using the FY-4A LST directly. Compared to FY-4A LST (FY-4A LST is used as a comparison standard), CLDAS LSTs in the central and western parts of the TP are significantly underestimated at 06:00 in DOY 001 and 361. In

the eastern part of TP, the spatial distribution of CLDAS LST is more consistent with FY-4A LST. The reconstructed AW LST and FY-4A LST maintain high consistency in magnitude and spatial patterns over the whole TP. In the region where CLDAS is underestimated, the spatial distribution of AW LST is more consistent with that of FY-4A LST. This finding indicates that RTG can suppress the underestimation of CLDAS LST, and the accuracy of AW LST is not affected when the CLDAS has a large uncertainty. RTG can also reconstruct the AW LST of the entire TP well during the day when the FY-4A LST pixels are almost completely missing due to the cloud cover *(e.g.*, 12:00 in DOY 001 and 241). In addition, we found that there is no obvious "boundary effect" between the clear-sky LST and cloudy-sky LST, indicating that the reconstructed AW LSTs possess good spatial continuity. Compared to CLDAS LST, the reconstructed AW LST has better image quality, higher spatial resolution (FY-4A LST and ancillary data have higher spatial resolutions), and higher spatial coverage (CLDAS LST has a significant spatial missing in some hours).

D. Discussion

Although this study develops an effective method to reconstruct a high-temporal resolution AW LST based on the reanalysis data and TIR data from geostationary satellites, an in-depth discussion is needed. First, the evaluation results based on *in-situ* LST indicate there are some obvious systematic errors in the FY-4A LSTs. Such systematic error may be further magnified in the reconstruction of the AW LST, affecting the accuracy of the AW LST under cloudy-sky conditions. Second, the CLDAS data also have some uncertainties, and some parameters (*e.g.*, LST) present spatial deficiencies. This also adds more uncertainty and errors to the AW LST reconstruction. In addition, it should be noted that CLDAS includes both near-real-time and real-time versions. Generally, near-real-time CLDAS has better quality compared to real-time CLDAS due to good post-processing and quality control. However, the near-real-time CLDAS in 2020 was not released when this study was being conducted. Thus, we used the archived data from the real-time CLDAS in this study. Third, fewer high-temporal resolution remote sensing parameters are used in the estimation of the AC, especially for the cloud parameters (quantitative parameters) that are unavailable. The absence of relevant parameters deteriorates the accuracy of the estimated all-weather AC to some extent.

According to the evaluation results in section IV A, it is clear that FY-4A and CLDAS LSTs have large uncertainty. To quantitatively evaluate the effect of uncertainty in two LSTs (*i.e.*, FY-4A and CLDAS LSTs) on the accuracy of the reconstructed AW LST, the following two control experiments are conducted.

In the first experiment, the clear-sky *in-situ* LST was input into RTG and then used to replace the FY-4A LST to reconstruct the AW LST for corresponding pixels at the six sites. The absolute difference in accuracy between the first reconstructed AW LST and the original AW LST was used to quantify the effect of the uncertainty in the FY-4A LST on the AW LST. In the second experiment, the all-weather *in-situ* LST was input into RTG and then used to replace the CLDAS LST to reconstruct the AW LST for corresponding pixels for the six sites. Similarly, the absolute difference in accuracy between the second reconstructed AW LST and the original AW LST was used to quantify the effect of the uncertainty in the CLDAS LST on the AW LST. The effects of uncertainties of two LSTs on the reconstruction results are shown in Fig. 13.

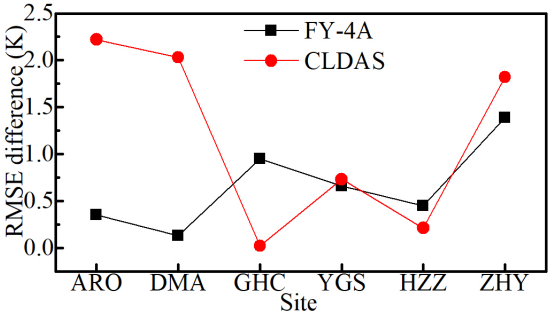

Fig. 13. The evaluation results of the impact of the uncertainty of the two input LSTs (*i.e.*, FY-4A LST and CLDAS LST) on reconstructed AW LST with RTG method.

FY-4A affects the accuracy of AW LST with a mean RMSE difference of about 0.66 K. For ZHY, FY-4A has the largest effect on AW LST with a mean RMSE difference of about 1.39 K. CLDAS affects the accuracy of AW LST with a mean RMSE difference of about 1.18 K. For ARO, DMA, and ZHY, CLDAS has a greater effect on AW LST than the other three sites, with the RMSE differences of 2.22 K, 2.03 K, and 1.82 K, respectively. Overall, CLDAS has a greater impact on the accuracy of the AW LST than the FY-4A. According to the principle of the RTG method, CLDAS is mainly used to estimate AC. Therefore, the estimation accuracy of AC is greatly affected by CLDAS. CLDAS has a further impact on the accuracy of AW LST. Nevertheless, the effects of both LST products on the AW LST are generally within the acceptable range.

In addition, some limitations should be noted. The accuracy of the AW LST depends on the FY-4A LST and CLDAS LST. In the future, if higher-quality geostationary satellite LST data and reanalysis data are available, the reconstructed AW LST will have better accuracy. At the same time, if more high-temporal resolution remote sensing parameters are further collected, the AC under cloudy-sky conditions can be estimated reasonably with the proposed RTG method.

V. Conclusions

All-weather LST (namely, AW LST) with a high temporal resolution is crucial in many studies and applications associated with the geoscience field. However, studies on how to obtain the AW LST with high quality are rare. In this study, a so-called RTG method is proposed to reconstruct the hourly AW LST by integrating reanalysis data and TIR data from geostationary satellites. RTG decomposes the LST into NC and AC components. On the one hand, the all-weather NC is initially determined based on the ATC model and then filled and optimized by employing the RF and DTC model. On the other hand, the all-weather AC is determined through time correction

and spatial weighting of the initial AC provided by CLDAS. By selecting the TP as the study area, RTG is applied to FY-4A LST and CLDAS data to reconstruct the hourly AW LST. Validation based on *in-situ* LST indicates that RMSEs (R^2) of the obtained hourly AW LST at 0.04° vary from 2.71 K (0.92) to 4.45 K (0.97) for clear-sky conditions, from 3.52 K (0.88) to 4.18 K (0.93) for cloudy-sky conditions, and from 3.12 K (0.92) to 4.33 K (0.96) for all-weather conditions. The results of the LST time series evaluation show that the AW LSTs are consistent with the *in-situ* LSTs, and the AW LSTs can also maintain a consistent change trend with the *in-situ* LSTs at the date of the LST mutation. The spatial patterns of AW LSTs show that RTG can effectively reconstruct the missing LST of FY-4A data without an obvious "boundary effect" caused by large missing areas. Overall, RTG can be flexibly extended to other geostationary satellites and reanalysis datasets. The hourly AW LST can better contribute to understand the regional diurnal LST variation and estimate remote sensing parameters, such as soil moisture, evaporation, and surface air temperature, with high temporal resolution.

ACKNOWLEDGMENT

The authors would like to thank the providers of the datasets used in this study, including the National Satellite Meteorological Center for FY-4A data, China Meteorological Data Service Centre for CLDAS data, the EARTH DATA for MODIS data, Goddard Earth Sciences Data and Information Services Center for GLDAS data, and USGS for the Landsat data. We also appreciate the Chinese colleagues for providing the ground measurements, as annotated in the paper. The authors acknowledge the contributions of the anonymous reviewers.

REFERENCES

[1] M. C. Anderson, J. M. Norman, W. P. Kustas, R. Houborg, P. J. Starks, and N. Agam, "A thermal-based remote sensing technique for routine mapping of land-surface carbon, water and energy fluxes from field to regional scales," *Remote Sens. Environ.*, vol. 112, no. 12, pp. 4227–4241, 2008, doi: https://doi.org/10.1016/j.rse.2008.07.009.

[2] P. Wu, H. Shen, L. Zhang, and F. M. Göttsche, "Integrated fusion of multi-scale polar-orbiting and geostationary satellite observations for the mapping of high spatial and temporal resolution land surface temperature," *Remote Sensing of Environment*, vol. 156. pp. 169–181, 2015. doi: 10.1016/j.rse.2014.09.013.

[3] H. Xia, Y. Chen, Y. Li, and J. Quan, "Combining kernel-driven and fusion-based methods to generate daily high-spatial-resolution land surface temperatures," *Remote Sens. Environ.*, vol. 224, pp. 259–274, 2019, doi: https://doi.org/10.1016/j.rse.2019.02.006.

[4] Z. Wang *et al.*, "A Land Surface Temperature Retrieval Method for UAV Broadband Thermal Imager Data," *IEEE Geosci. Remote Sens. Lett.*, vol. 19, pp. 1–5, 2021.

[5] S. Sruthi and M. A. M. Aslam, "Agricultural Drought Analysis Using the NDVI and Land Surface Temperature Data; a Case Study of Raichur District," *Aquat. Procedia*, vol. 4, pp. 1258–1264, 2015, doi: 10.1016/j.aqpro.2015.02.164.

[6] L. Zhang, W. Jiao, H. Zhang, C. Huang, and Q. Tong, "Studying drought phenomena in the Continental United States in 2011 and 2012 using various drought indices," *Remote Sens. Environ.*, vol. 190, pp. 96–106, 2017, doi: 10.1016/j.rse.2016.12.010.

[7] Q. Meng, L. Zhang, Z. Sun, F. Meng, L. Wang, and Y. Sun, "Characterizing spatial and temporal trends of surface urban heat island effect in an urban main built-up area: A 12-year case study in Beijing, China," *Remote Sens. Environ.*, vol. 204, pp. 826–837, 2018, doi: 10.1016/j.rse.2017.09.019.

[8] J. Quan, Y. Chen, W. Zhan, J. Wang, J. Voogt, and M. Wang, "Multi-temporal trajectory of the urban heat island centroid in Beijing, China based on a Gaussian volume model," *Remote Sens. Environ.*, vol. 149, pp. 33–46, 2014, doi: 10.1016/j.rse.2014.03.037.

[9] X. Zhu, X. Wang, D. Yan, Z. Liu, and Y. Zhou, "Analysis of remotely-sensed ecological indexes' influence on urban thermal environment dynamic using an integrated ecological index: a case study of Xi'an, China," *Int. J. Remote Sens.*, vol. 40, no. 9, pp. 3421–3447, 2019.

[10] X.-M. Zhu, X.-N. Song, P. Leng, D. Guo, and S.-H. Cai, "Impact of atmospheric correction on spatial heterogeneity relations between land surface temperature and biophysical compositions," *IEEE Trans. Geosci. Remote Sens.*, vol. 59, no. 3, pp. 2680–2697, 2020.

[11] L. Bai, D. Long, and L. Yan, "Estimation of Surface Soil Moisture With Downscaled Land Surface Temperatures Using a Data Fusion Approach for Heterogeneous Agricultural Land," *Water Resour. Res.*, vol. 55, no. 2, pp. 1105–1128, 2019, doi: 10.1029/2018WR024162.

[12] L. Song *et al.*, "Monitoring and validating spatially and temporally continuous daily evaporation and transpiration at river basin scale," *Remote Sens. Environ.*, vol. 219, pp. 72–88, 2018, doi: 10.1016/j.rse.2018.10.002.

[13] W. P. Kustas *et al.*, "Revisiting the paper 'Using radiometric surface temperature for surface energy flux estimation in Mediterranean drylands from a two-source perspective,'" *Remote Sens. Environ.*, vol. 184, pp. 645–653, 2016, doi: 10.1016/j.rse.2016.07.024.

[14] S. Liang, K. Wang, X. Zhang, and M. Wild, "Review on Estimation of Land Surface Radiation and Energy Budgets From Ground Measurement, Remote Sensing and Model Simulations," *IEEE J. Sel. Top. Appl. Earth Obs. Remote Sens.*, vol. 3, no. 3, pp. 225–240, Sep. 2010, doi: 10.1109/JSTARS.2010.2048556.

[15] T. W. Ford and S. M. Quiring, "Comparison of Contemporary In Situ, Model, and Satellite Remote Sensing Soil Moisture With a Focus on Drought Monitoring," *Water Resour. Res.*, vol. 55, no. 2, pp. 1565–1582, 2019, doi: 10.1029/2018WR024039.

[16] Z. L. Li *et al.*, "Satellite-derived land surface temperature: Current status and perspectives," *Remote Sens. Environ.*, vol. 131, pp. 14–37, 2013, doi: 10.1016/j.rse.2012.12.008.

[17] Y.-Z. Zhang, H. Wu, X.-G. Jiang, Y.-Z. Jiang, Z.-X. Liu, and F. Nerry, "Land surface temperature and emissivity retrieval from field-measured hyperspectral thermal infrared data using wavelet transform," *Remote Sens.*, vol. 9, no. 5, p. 454, 2017.

[18] D. Long *et al.*, "Generation of spatially complete and daily continuous surface soil moisture of high spatial resolution," *Remote Sens. Environ.*, vol. 233, pp. 111364–111364, 2019, doi: 10.1016/j.rse.2019.111364.

[19] Q. Weng and P. Fu, "Modeling annual parameters of clear-sky land surface temperature variations and evaluating the impact of cloud cover using time series of Landsat TIR data," *Remote Sens. Environ.*, vol. 140, pp. 267–278, 2014, doi: 10.1016/j.rse.2013.09.002.

[20] F. J. Wentz, C. Gentemann, D. Smith, and D. Chelton, "Satellite measurements of sea surface temperature through clouds.," *Science*, vol. 288, no. 5467, pp. 847–850, May 2000, doi: 10.1126/science.288.5467.847.

[21] T. I. Østby, T. V. Schuler, and S. Westermann, "Severe cloud contamination of MODIS Land Surface Temperatures over an Arctic ice cap, Svalbard," *Remote Sens. Environ.*, vol. 142, pp. 95–102, 2014, doi: 10.1016/j.rse.2013.11.005.

[22] P. Jonsson and L. Eklundh, "Seasonality extraction by function fitting to time-series of satellite sensor data," *IEEE Trans. Geosci. Remote Sens.*, vol. 40, no. 8, pp. 1824–1832, 2002.

[23] X. Lu, R. Liu, J. Liu, and S. Liang, "Removal of noise by wavelet method to generate high quality temporal data of terrestrial MODIS products," *Photogramm. Eng. Remote Sens.*, vol. 73, no. 10, pp. 1129–1139, 2007.

[24] J. P. Scharlemann *et al.*, "Global data for ecology and epidemiology: a novel algorithm for temporal Fourier processing MODIS data," *PloS One*, vol. 3, no. 1, p. e1408, 2008.

[25] G. Zhang *et al.*, "Mapping paddy rice planting areas through time series analysis of MODIS land surface temperature and vegetation index data," *ISPRS J. Photogramm. Remote Sens.*, vol. 106, pp. 157–171, 2015.

[26] M. Neteler, "Estimating daily land surface temperatures in mountainous environments by reconstructed MODIS LST data," *Remote Sens.*, vol. 2, no. 1, pp. 333–351, 2010.

[27] P. Wu *et al.*, "Spatially Continuous and High-Resolution Land Surface Temperature Product Generation: A Review of Reconstruction and

Spatiotemporal Fusion Techniques," *IEEE Geosci. Remote Sens. Mag.*, 2021.

[28] Z. Liu, P. Wu, S. Duan, W. Zhan, X. Ma, and Y. Wu, "Spatiotemporal Reconstruction of Land Surface Temperature Derived From FengYun Geostationary Satellite Data," *IEEE J. Sel. Top. Appl. Earth Obs. Remote Sens.*, vol. 10, no. 10, pp. 4531–4543, Oct. 2017, doi: 10.1109/JSTARS.2017.2716376.

[29] L. Sun *et al.*, "Reconstructing daily clear-sky land surface temperature for cloudy regions from MODIS data," *Comput. Geosci.*, vol. 105, pp. 10–20, 2017, doi: 10.1016/j.cageo.2017.04.007.

[30] Q. Weng, P. Fu, and F. Gao, "Generating daily land surface temperature at Landsat resolution by fusing Landsat and MODIS data," *Remote Sens. Environ.*, vol. 145, pp. 55–67, 2014.

[31] J. Zeng, Z. Li, Q. Chen, and H. Bi, "Method for Soil Moisture and Surface Temperature Estimation in the Tibetan Plateau Using Spaceborne Radiometer Observations," *IEEE Geosci. Remote Sens. Lett.*, vol. 12, no. 1, pp. 97–101, Jan. 2015, doi: 10.1109/LGRS.2014.2326890.

[32] M. Metz, D. Rocchini, and M. Neteler, "Surface temperatures at the continental scale: tracking changes with remote sensing at unprecedented detail," *Remote Sens.*, vol. 6, no. 5, pp. 3822–3840, 2014.

[33] M. Jin, "Interpolation of surface radiative temperature measured from polar orbiting satellites to a diurnal cycle: 2. Cloudy-pixel treatment," *J. Geophys. Res. Atmospheres*, vol. 105, no. D3, pp. 4061–4076, 2000.

[34] J. Martins *et al.*, "An all-weather land surface temperature product based on MSG/SEVIRI observations," *Remote Sens.*, vol. 11, no. 24, p. 3044, 2019.

[35] W. Zhao and S.-B. Duan, "Reconstruction of daytime land surface temperatures under cloud-covered conditions using integrated MODIS/Terra land products and MSG geostationary satellite data," *Remote Sens. Environ.*, vol. 247, p. 111931, 2020.

[36] S.-B. Duan, Z.-L. Li, and P. Leng, "A framework for the retrieval of all-weather land surface temperature at a high spatial resolution from polar-orbiting thermal infrared and passive microwave data," *Remote Sens. Environ.*, vol. 195, pp. 107–117, Jun. 2017, doi: 10.1016/J.RSE.2017.04.008.

[37] X. Zhang, J. Zhou, F. M. Gottsche, W. Zhan, S. Liu, and R. Cao, "A Method Based on Temporal Component Decomposition for Estimating 1-km All-Weather Land Surface Temperature by Merging Satellite Thermal Infrared and Passive Microwave Observations," *IEEE Trans. Geosci. Remote Sens.*, vol. 57, no. 7, pp. 4670–4691, 2019, doi: 10.1109/TGRS.2019.2892417.

[38] S. Xu, J. Cheng, and Q. Zhang, "Reconstructing All-Weather Land Surface Temperature Using the Bayesian Maximum Entropy Method Over the Tibetan Plateau and Heihe River Basin," *IEEE J. Sel. Top. Appl. Earth Obs. Remote Sens.*, vol. 12, no. 9, pp. 3307–3316, 2019.

[39] X. Zhang, J. Zhou, S. Liang, L. Chai, D. Wang, and J. Liu, "Estimation of 1-km all-weather remotely sensed land surface temperature based on reconstructed spatial-seamless satellite passive microwave brightness temperature and thermal infrared data," *ISPRS J. Photogramm. Remote Sens.*, vol. 167, pp. 321–344, 2020, doi: 10.1016/j.isprsjprs.2020.07.014.

[40] S. Xu and J. Cheng, "A new land surface temperature fusion strategy based on cumulative distribution function matching and multiresolution Kalman filtering," *Remote Sens. Environ.*, vol. 254, p. 112256, 2021.

[41] D. Long *et al.*, "Generation of MODIS-like land surface temperatures under all-weather conditions based on a data fusion approach," *Remote Sens. Environ.*, vol. 246, pp. 111863–111863, 2020, doi: 10.1016/j.rse.2020.111863.

[42] X. Zhang, J. Zhou, S. Liang, and D. Wang, "A practical reanalysis data and thermal infrared remote sensing data merging (RTM) method for reconstruction of a 1-km all-weather land surface temperature," *Remote Sens. Environ.*, vol. 260, p. 112437, 2021, doi: https://doi.org/10.1016/j.rse.2021.112437.

[43] Y. Jiang and Q. Weng, "Estimation of hourly and daily evapotranspiration and soil moisture using downscaled LST over various urban surfaces," *GIScience Remote Sens.*, vol. 54, no. 1, pp. 95–117, 2017.

[44] Q. Weng and P. Fu, "Modeling diurnal land temperature cycles over Los Angeles using downscaled GOES imagery," *ISPRS J. Photogramm. Remote Sens.*, vol. 97, pp. 78–88, 2014.

[45] L. Ding, J. Zhou, X. Zhang, S. Liu, and R. Cao, "Downscaling of surface air temperature over the Tibetan Plateau based on DEM," *Int. J. Appl. Earth Obs. Geoinformation*, vol. 73, pp. 136–147, 2018, doi: 10.1016/j.jag.2018.05.017.

[46] T. Yao *et al.*, "Different glacier status with atmospheric circulations in Tibetan Plateau and surroundings," *Nat. Clim. Change*, vol. 2, no. 9, pp. 663–667, 2012.

[47] C. Ulivieri and G. Cannizzaro, "Land surface temperature retrievals from satellite measurements," *Acta Astronaut.*, vol. 12, no. 12, pp. 977–985, 1985.

[48] X. Wang, M. Min, F. Wang, J. Guo, B. Li, and S. Tang, "Intercomparisons of cloud mask products among Fengyun-4A, Himawari-8, and MODIS," *IEEE Trans. Geosci. Remote Sens.*, vol. 57, no. 11, pp. 8827–8839, 2019.

[49] R. J. Joyce, J. E. Janowiak, P. A. Arkin, and P. Xie, "CMORPH: A method that produces global precipitation estimates from passive microwave and infrared data at high spatial and temporal resolution," *J. Hydrometeorol.*, vol. 5, no. 3, pp. 487–503, 2004.

[50] C. X. Shi, Z. H. Xie, Q. Hui, M. L. Liang, and X. C. Yang, "China land soil moisture EnKF data assimilation based on satellite remote sensing data," *Sci. China Earth Sci.*, vol. 54, no. 9, pp. 1430–1440, 2011.

[51] B. Jia, Z. Xie, A. Dai, C. Shi, and F. Chen, "Evaluation of satellite and reanalysis products of downward surface solar radiation over East Asia: Spatial and seasonal variations," *J. Geophys. Res. Atmospheres*, vol. 118, no. 9, pp. 3431–3446, 2013.

[52] X. Li *et al.*, "Heihe Watershed Allied Telemetry Experimental Research (HiWATER): Scientific Objectives and Experimental Design," *Bull. Am. Meteorol. Soc.*, vol. 94, no. 8, Art. no. 8, 2013.

[53] S. M. Liu *et al.*, "A comparison of eddy-covariance and large aperture scintillometer measurements with respect to the energy balance closure problem," *Hydrol. Earth Syst. Sci.*, vol. 15, no. 4, pp. 1291–1306, 2011.

[54] S. Liu *et al.*, "The Heihe Integrated Observatory Network: A basin-scale land surface processes observatory in China," *Vadose Zone J.*, vol. 17, no. 1, pp. 1–21, 2018.

[55] X. Li *et al.*, "Qinghai Lake Basin Critical Zone Observatory on the Qinghai-Tibet Plateau," *Vadose Zone J.*, vol. 17, no. 1, pp. 1–11, 2018.

[56] X.-Y. Li *et al.*, "Evaporation and surface energy budget over the largest high-altitude saline lake on the Qinghai-Tibet Plateau," *J. Geophys. Res. Atmospheres*, vol. 121, no. 18, pp. 10–470, 2016.

[57] K. Wang and S. Liang, "Global atmospheric downward longwave radiation over land surface under all-sky conditions from 1973 to 2008," *J. Geophys. Res. Atmospheres*, vol. 114, no. D19, Art. no. D19, 2009.

[58] S. Liang, *Quantitative remote sensing of land surfaces*, vol. 30. John Wiley & Sons, 2005.

[59] H. Li *et al.*, "Evaluation of the VIIRS and MODIS LST products in an arid area of Northwest China," *Remote Sens. Environ.*, vol. 142, pp. 111–121, 2014.

[60] J. Ma *et al.*, "Continuous evaluation of the spatial representativeness of land surface temperature validation sites," *Remote Sens. Environ.*, vol. 265, p. 112669, 2021.

[61] J. Zhou, J. Li, L. Zhang, D. Hu, and W. Zhan, "Intercomparison of methods for estimating land surface temperature from a Landsat-5 TM image in an arid region with low water vapour in the atmosphere," *Int. J. Remote Sens.*, vol. 33, no. 8, pp. 2582–2602, Apr. 2012, doi: 10.1080/01431161.2011.617396.

[62] W. Zhan *et al.*, "Remotely sensed soil temperatures beneath snow-free skin-surface using thermal observations from tandem polar-orbiting satellites: An analytical three-time-scale model," *Remote Sens. Environ.*, vol. 143, pp. 1–14, Mar. 2014, doi: 10.1016/J.RSE.2013.12.004.

[63] B. Bechtel, Bechtel, and Benjamin, "A New Global Climatology of Annual Land Surface Temperature," *Remote Sens.*, vol. 7, no. 3, pp. 2850–2870, Mar. 2015, doi: 10.3390/rs70302850.

[64] J. Zhou, Y. Chen, J. Wang, and W. Zhan, "Maximum nighttime urban heat island (UHI) intensity simulation by integrating remotely sensed data and meteorological observations," *IEEE J. Sel. Top. Appl. Earth Obs. Remote Sens.*, vol. 4, no. 1, pp. 138–146, 2011.

[65] J. Chen, X. Zhu, J. E. Vogelmann, F. Gao, and S. Jin, "A simple and effective method for filling gaps in Landsat ETM+ SLC-off images," *Remote Sens. Environ.*, vol. 115, no. 4, pp. 1053–1064, 2011, doi: 10.1016/j.rse.2010.12.010.

[66] F.-M. Göttsche *et al.*, "Long Term Validation of Land Surface Temperature Retrieved from MSG/SEVIRI with Continuous in-Situ Measurements in Africa," *Remote Sens.*, vol. 8, no. 5, pp. 410–410, May 2016, doi: 10.3390/rs8050410.

[67] R. K. Pearson, "Outliers in Process Modeling and Identification," *IEEE Trans. Geosci. Remote Sens.*, vol. 10, no. 1, pp. 55–63, 2002.